available at www.sciencedirect.com

ScienceDirect

journal homepage: www.sciencedirect.com/journal/chinese-journal-of-catalysis

Review

Fundamental aspects in CO_2 electroreduction reaction and solutions from *in situ* vibrational spectroscopies

Hong Li [a], Kun Jiang [b], Shou-Zhong Zou [c,#], Wen-Bin Cai [a,*]

[a] *Shanghai Key Laboratory of Molecular Catalysis and Innovative Materials, Collaborative Innovation Center of Chemistry for Energy Materials, Department of Chemistry, Fudan University, Shanghai 200438, China*

[b] *School of Mechanical Engineering, Shanghai Jiao Tong University, Shanghai 200240, China*

[c] *Department of Chemistry, American University, Washington, District of Columbia 20016, United States*

ARTICLE INFO

Article history:
Received 31 January 2022
Accepted 27 March 2022
Available online 5 xxxxxx 2021

Keywords:
Carbon dioxide electroreduction reaction
Electrocatalytic mechanism
Vibrational spectroscopy
Intermediate
Structure-performance relation
Electrolyte effect

ABSTRACT

Using renewable energy to drive carbon dioxide reduction reaction (CO_2RR) electrochemically into chemicals with high energy density is an efficient way to achieve carbon neutrality, where the effective utilization of CO_2 and the storage of renewable energy are realized. The reactivity and selectivity of CO_2RR depend on the structure and composition of the catalyst, applied potential, electrolyte, and pH of the solution. Besides, multiple electron and proton transfer steps are involved in CO_2RR, making the reaction pathways even more complicated. In pursuit of molecular-level insights into the CO_2RR processes, *in situ* vibrational methods including infrared, Raman and sum frequency generation spectroscopies have been deployed to monitor the dynamic evolution of catalyst structure, to identify reactive intermediates as well as to investigate the effect of local reaction environment on CO_2RR performance. This review sumarizes key findings from recent electrochemical vibrational spectrosopic studies of CO_2RR in addressing the following issues: the CO_2RR mechanisms of different pathways, the role of surface-bound CO species, the compositional and structural effects of catalysts and electrolytes on CO_2RR activity and selectivity. Our perspectives on developing high sensitivity wide-frequency infrared spectroscopy, coupling different spectroelectrochemical methods and implementing operando vibrational spectroscopies to tackle the CO_2RR process in pilot reactors are offered at the end.

1. Introduction

Electroreduction of CO_2 is promising in mitigating the green house and achieving carbon neutrality [1,2]. It is envisioned that the electricity generated by renewable energy is used to convert CO_2 into value-added fuels, and the stored energy in these chemicals can be released as electricity through fuel cells or as other forms of energy [3–5]. Such a practice can not only realize the storage of renewable energy, but also mitigate the anthropogenic CO_2 emission. Considerable efforts have been devoted to CO_2RR and great progress has been made in catalysts, reaction mechanisms, and reaction devices [6,7]. Strategies of improving the product selectivity and overall reaction activity, such as constructing grain boundaries, controlling crystal facets, forming unsaturated coordination sites or alloys, doping transition metals with non-metallic elements, and sur-

* Corresponding author. Tel/Fax: +86-21-31244050; E-mail: wbcai@fudan.edu.cn
# Corresponding author. Tel/Fax: +202-885-1763; E-mail: szou@american.edu

This work was supported by the National Natural Science Foundation of China (21733004, 22002088) , the International Cooperation Program of Shanghai Science and Technology Committee (17520711200), and the Shanghai Sailing Program (20YF1420500).
DOI: 10.1016/S1872-2067(22)64095-6 | http://www.sciencedirect.com/journal/chinese-journal-of-catalysis | Chin. J. Catal., Vol. 43, No. 0, xxxxxx 2022

face modification, have been extensively explored [8–12]. A large number of works have been focused on elucidating the structure-performance relationship between different crystallographic planes and electrocatalytic activity and selectivity [3,13,14]. The effects of different electrode potentials, electrolytes, and solution pH on the performance of CO_2RR have also been studied [15,16]. The key intermediates such as *CHO or *OCCO for the formation of the C_1 and C_2 products were deduced through experiments and theoretical calculations [17,18]. In addition, flow cell and membrane electrode assembly (MEA) systems were also developed to improve the current density of CO_2RR and accelerate the practical application of this process [19–22]. Developments along these lines have been summarized in many recent reviews [3,4,6,7,10–12,14,18,23].

Despite the tremendous amount of work on CO_2RR, the reaction mechanism together with the structural effects of catalysts and electrolytes remain elusive. These challenges arise in part because the reaction is complex involving multiple electron and proton transfer steps, and in part from the dynamic change of the interfacial structure on both the solution and the catalyst surface sides. To tackle these challenges, *in situ* characterization methods that are able to monitor the evolution of catalyst structures in real time during the reaction process, identify catalyst active sites, probe the reaction microenvironment, and capture key reaction intermediates have been employed [24–27]. Among them, *in-situ* vibrational spectroscopy has high sensitivity and interfacial selectivity, and can monitor the catalyst structure reconstruction and the dynamic evolution of adsorbed species during the CO_2 reduction reaction, providing important information for clarifying the reaction mechanism and reaction pathways of CO_2RR, as demonstrated in previous work [25,26,28–31]. Although many reviews on CO_2RR have appeared in the past decade, few of them focused on fundamental problem-solving targeted application of *in situ* vibrational spectroscopic approaches. Given the critical information garnered from these methods for fundamental understanding of CO_2RR, it is our hope that a review on this topic may stimulate further application and advancement of using *in situ* vibrational spectroscopic methods in CO_2RR studies.

This review summarizes representative results from *in situ* vibrational spectroscopic studies on key fundamental issues in CO_2RR (Fig. 1), including (1) the reaction pathways and intermediates; (2) the roles of adsorbed CO; (3) the effects of catalyst structure and (4) the effects of electrolyte. At the end, we provide brief outlooks of the future directions for *in situ* spectroscopic investigation of CO_2RR.

2. Brief introduction of *in situ* vibrational spectroscopy

The study of microscopic CO_2RR mechanisms strongly relies on the identification of intermediates and products for different pathways. *In situ* vibrational spectroscopy with high sensitivity and surface specificity can reveal the dynamic chemical nature of adsorbed intermediates in milliseconds, which is critical to study the electrocatalytic reaction mechanism. Vibrational spectroscopic techniques include infrared absorption spectroscopy (IR), Raman scattering spectroscopy, and sum frequency generation spectroscopy (SFG), with corresponding schematic setup shown in Fig. 2. These techniques provide complementary molecular information about the interfacial processes involved in the CO_2RR.

Wen-Bin Cai *(Department of Chemistry, Fudan University) received his B.A. degree and M.S. degree from Shanghai University of Science and Technology in 1989 and 1992, respectively, under the guidance of Prof. Xun-Nan Deng and Ph.D. degree from Fudan University in 1995 under the guidance of Prof. Wei-Fang Zhou. From 1995 to 2002, he did postdoctoral research work consecutively at Xiamen University (with Prof. Zhong-Qun Tian), Hokkaido University (with Prof. Masatoshi Osawa), and Case Western Reserve University (with Profs. Daniel Scherson and James Burgess). Since July, 2002, he has been a professor at Fudan University. His research interests cover interfacial spectroelectrochemistry and electrocatalysis, including but not limited to methodological development and application of electrochemical ATR-SEIRAS, mechanistic understanding and catalyst development towards electrocatalysis of small organic molecule oxidation, oxygen reduction and carbon dioxide reduction.*

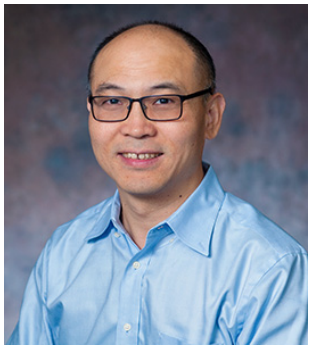

Shouzhong Zou *(Department of Chemistry, American University) earned his B.S. in Chemistry in 1991 and completed his MS studies in 1994 from Xiamen University under the guidance of Prof. Zhong-Qun Tian. He received his Ph.D. in Chemistry from Purdue University in 1999 under the direction of Prof. Michael J. Weaver. He then did postdoctoral work at Caltech with Profs. Fred C Anson and Ahmed H. Zewail. He started his independent research as an assistant professor in 2002 at Miami University (Oxford, Ohio), and was promoted to associate professor in 2008. He joined American University in the summer of 2015 as a full professor and chair. His research interests include developing catalysts for low temperature fuel cells, CO_2 reduction and gas sensing, and advancing spectroscopic and microscopic techniques for the characterization of surfaces and interfaces.*

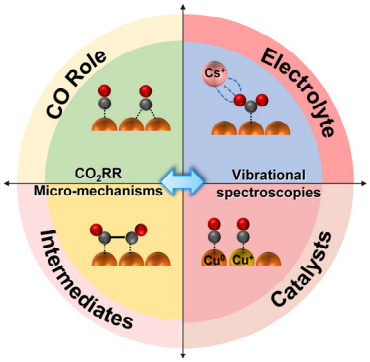

Fig. 1. Fundamental issues for the electrochemical reduction of CO_2.

2.1. *Electrochemical infrared spectroscopy*

In recent years, electrochemical-surface-enhanced infrared spectroscopy has played an important role in exploring various interfacial phenomena in CO_2 electroreduction reactions [29,30,34]. Infrared spectroscopy exploits the specific absorption of infrared radiation at the resonant frequencies of molecular vibrations and can be used to monitor functional groups, molecular symmetry, and interactions between catalysts and molecules [35]. It has the advantages of being applicable to most metals, good spectral signal reversibility, simple surface selection rules and high sensitivity to polar molecules. Electrochemical infrared spectroscopy uses two main modes [36,37]: internal reflection-absorption or attenuated total reflection and external reflection-absorption modes. In ATR mode (Fig. 2(a)), the working electrode is either a metal (Au, Ag or Cu) film with a thickness of about 10–100 nm deposited on the reflective plane of a Si or Ge infrared window [38–40], or a powder catalyst layer cast Au films. In this mode, the infrared light impinges on the metal from the back side and the penetration depth of infrared waves through metal is small. It is therefore particularly sensitive to adsorbed species on the electrode surface. With this mode the mass transfer is fast and it is beneficial for tracking dynamic process, especially for the study of surface processes with a large amount of gas evolution, but it is difficult to detect low concentration soluble species due to its limited penetration depth. In the external reflection mode, the incident infrared light passes through the solution before reaches the electrode surface. The working electrode can be a metal thin film deposited on a support electrode or a polished metal electrode. To minimize the absorption of water and other species in the bulk solution, the electrode is usually pushed against the infrared window forming a thin solution layer (~ a few microns) sandwiched between the window and the electrode surface. The external reflection mode is beneficial for the detection of solution-phase species, such as soluble intermediates and products, but its hindered mass transport is not conducive to the study of dynamic CO_2RR processes [31].

2.2. *Electrochemical Raman spectroscopy*

Raman spectroscopy offers high sensitivity in the low wavenumber region where surface-adsorbate stretch and metal oxide phonon modes are located [41]. Due to the low water scattering, Raman spectroscopy can be applied to aqueous environment without the need of spectral subtraction to remove the background (Fig. 2(b)). The combination of Raman and infrared spectroscopy provides complementary information on molecular structure and catalyst surface structure. In Raman spectroscopy, inelastically scattered light generated from the interaction of a monochromatic laser beam with a sample is the signal [42]. Since the signal of Raman scattering is very weak, roughened or nanostructured electrodes with surface enhancement effect mainly from the surface plasmon reasonance are generally used [43,44]. This approach is collectively called surface-enhanced Raman spectroscopy (SERS), which broadly speaking includes recently developed shell isolated nanoparticles enhanced Raman spectroscopy (SHINERS) that is able to obtain SERS signals from single crystal metal surfaces in contact with Au@SiO_2 nanoparticles [43].

Surface enhancement is highly demanded in both *in situ* Raman and IR spectroscopies for studying CO_2RR mechansims. In comparison to surface enhanced Raman scattering spectroscopy, surface enhanced infrared absorption spectroscopy (SEIRAS) has a more straightforward surface selection rule and is more sensitive to those adsorbates with larger dipole-moment change but smaller polarizability change. SEIRAS is also applicable to more metal electrodes because infrared radiation instead of visible light is used for exciting surface plasmon resonance of metal nanoparticles.

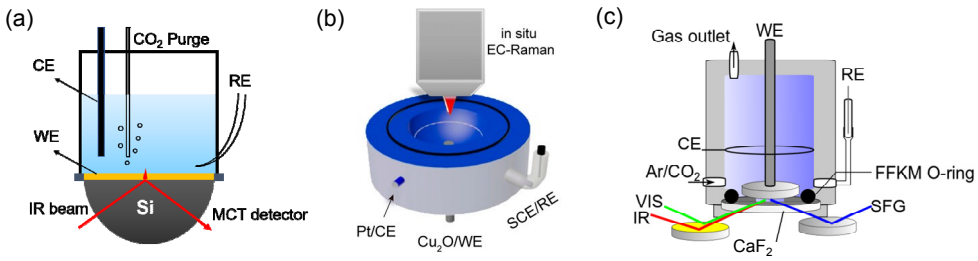

Fig. 2. The schematic setup of electrochemical attenuated total reflection (ATR) infrared spectroscopy (a) and Raman spectrocopy (b). Reprinted with permission from Ref. [32]. Copyright 2020, Proceedings of the National Academy of Sciences. (c) Sum-frequency generation spectroscopy. Reprinted with permission from Ref. [33]. Copyright 2019, American Chemical Society. Note: WE refers to Working Electrode, RE to Reference Electrode and CE to Counter Electrode.

2.3. Electrochemical sum-frequency generation spectroscopy

As a second-order nonlinear spectroscopy, sum frequency generation spectroscopy has unique interfacial selectivity and sensitivity, and can provide molecular information at the electrode/electrolyte interface, including molecular orientation [45,46]. In a typical vibrational SFG experiment, a visible laser beam and an infrared laser beam impringe on the surface from different incident angles [47]. These lights interact with the sample and generate a nonlinear polarization, then a third beam at the sum frequency of the incident beams is emitted (Fig. 2(c)) [33]. When the infrared laser frequency is in resonance with molecular vibrational frequency, the SFG signal is significantly enhanced and therefore molecular information is provided. Compared to infrared spectroscopy and Raman spectroscopy, SFG does not require background subtraction and roughened metal electrodes, since only surface species with non-centrosymmetric can be detected. Despite its unique advantage, this technique is very complicated in terms of optics, operation and spectral interpretation, and thus has not been widely used.

3. Reaction pathways and intermediates

Hori *et al.* [48] divided metals into four categories according to the different CO_2RR products generated from these metal electrodes. (1) In, Sn, Cd, Pb, Bi and Hg for fomate; (2) Au, Ag, Zn and Pd for CO; (3) Pt and Ni for H_2; (4) Cu for CH_4 and multi-carbon products (C_{2+}). Bagger *et al.* [49] performed theoretical simulations on the adsorption energies of each metal with *H and *CO, and predicted the corresponding CO_2 reduction products, which were consistent with Hori's experimental results. Since the products of CO_2RR are metal-dependent, the reaction mechanisms naturally differ. Using *in situ* infrared spectroscopy and theoretical calculations, Katayama *et al.* [50] proposed comprehensive CO_2RR reaction mechanisms for different metals. The study found that the reaction pathway of CO_2RR depends on the binding energy of metal to C or O. The formation of C1 products requires high binding capacity of the catalyst with the O-terminal intermediate, while the formation of C_{2+} products requires an optimal binding capacity of the catalyst with the C-terminal intermediate. Based on the theoretical studies, Goddard and coworkers [51,52] proposed that *HCOO and *COOH are intermediates, if the products are formic acid and CO, respectively. If the products are methane and C_{2+}, *CO is the intermediate. A simplified flowchart of the CO_2RR mechanisms is shown in Fig. 3. In this section, the application of vibrational spectroscopies in exploring the CO_2RR mechanism and key reaction intermediates that branch CO_2RR product distribution over different metal electrodes are discussed following this flowchart.

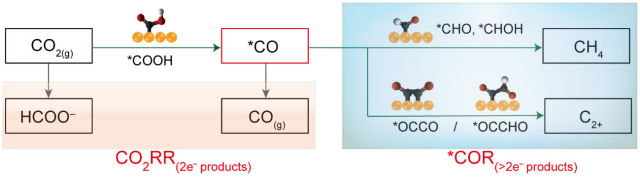

Fig. 3. Simplified flowchart of CO_2RR mechanisms leading to C1 and C_{2+} product generation. * Corresponds to adsorbed species, >2e⁻ reduction products of CH_4 and C_{2+} that go through the reduction of *CO intermediate (*COR) are marked in light blue. Reprinted with permission from Ref. [52]. Copyright 2020, American Chemical Society.

3.1. CO_2-to-formate conversion

The main product of CO_2RR on Sn, In, Pb, and Bi electrodes is formate. There are several speculations about the intermediates for the generation of formate. The monodentate OCHO* through the terminal O or *COOH through the terminal C has been suggested as the intermediate [18,53–55]. In practice, the formate formation mechanism as well as the spectral detection depends on the electrode composition and structure. To pin down the reaction mechansim, Baruch *et al.* [53] used *in situ* attenuated total reflectance infrared spectroscopy (ATR-IR) to study CO_2RR to formate on Sn electrodes containing oxide species, which the Faradaic efficiency (FE) of formate was ~45% at –1.4 V *vs.* RHE. Monodentate carbonate species on Sn oxide with vibrational bands located at 1500, 1385 and 1100 cm^{-1} were observed, and it was postulated that this speices is a key intermediate involved in the CO_2RR. (Fig. 4(a)). When the potential was stepped to –1.8 V *vs.* RHE and CO_2 was purged by Ar, the signal of carbonate species gradually decreased, confirming that the carbonate species adsorbed on the surface were the reaction intermediates. The authors found that this carbonate species is associated with oxides on Sn. When the oxide on the electrode is reduced or etched with acid, the signal of the carbonate species adsorbed on the surface disappeared, and the product is mainly H_2. Notably, infrared spectroscopy cannot provide information about oxide species on electrodes with vibration bands at low wavenumbers, while Raman spectroscopy can. Dutta *et al.* [56] used *in situ* Raman spectroscopy to demonstrate the correlation of oxidation state of the Sn oxide nanoparticles and the selective formation of formate in CO_2RR. A Raman peak at 623 cm^{-1} was assigned to the A_{1g} vibrational mode of SnO_2 crystallite. The intensity of the SnO_2-related A_{1g} modes changed with the applied electrode potential during CO_2RR. The high FE of formate was obtained when SnO_2 was the main catalytic species at low overpotentials. However, as the SnO_2 was partially or fully reduced to metallic Sn at very negative potentials, the FE of formate and the intensity of the SnO_2-related A_{1g} sharply decreased. These observations are consistent with Baruch's using infrared spectroscopy, which further support the conjecture that the surface oxide species on Sn electrodes is critical in the formation of formate. Pander *et al.* [54] found that the reaction pathway of CO_2 reduction to formate on In electrode is similar to Sn electrode (Fig. 4(b)), where the oxide species interact with CO_2 to form a metal-carbonate species, which is reduced to formate. For Pb and Bi electrodes, neither carbonate nor other adsorbed species ($HCOO_{ads}$) was detected by infrared spectroscopy [54], which suggests that Pb and Bi reduce CO_2 to formate through a different mechanism, and the reactive sites may be metallic Pb

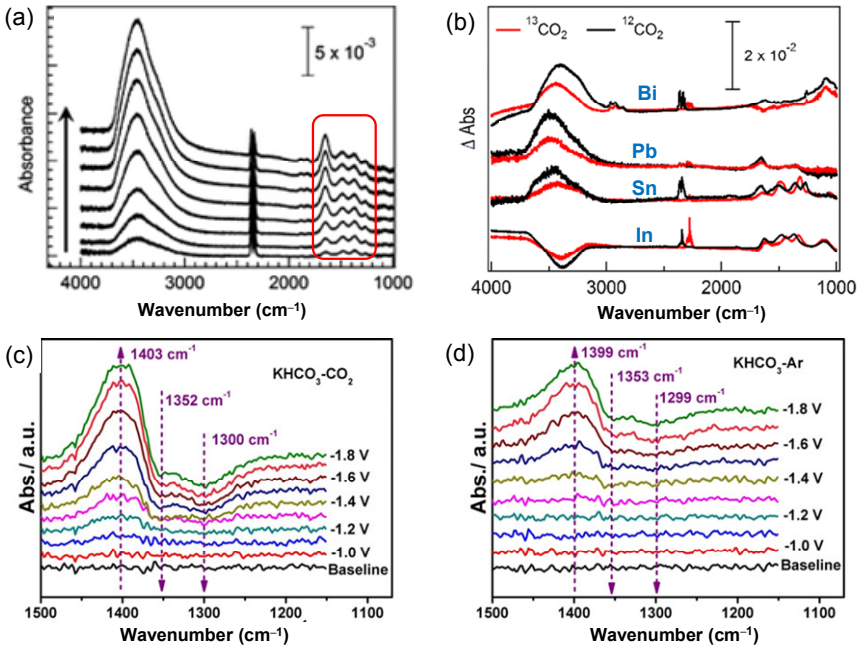

Fig. 4. (a) *In situ* time-dependent ATR-IR spectra of CO_2RR on Sn electrodes at –1.4 V *vs.* Ag/AgCl in 0.1 mol/L K_2SO_4 solution saturated with CO_2. The black arrow shows the direction of evolution with time and the red frame shows the carbonate species. Reprinted with permission from Ref. [53]. Copyright 2015, American Chemical Society. (b) ATR-IR spectra of thin films of indium, tin, lead, and bismuth on exposure to CO_2 under reducing conditions. Reprinted with permission from Ref. [54]. Copyright 2016, American Chemical Society. *In situ* ATR-SEIRAS collected under different applied potentials in CO_2 saturated (c) and Ar-saturated (d) 0.5 mol/L $KHCO_3$. Reprinted with permission from Ref. [55]. Copyright 2020, John Wiley and Sons.

or Bi rather than oxides (Fig. 4(b)). In fact, the formation of formate is possibly through a direct one-step electron transfer hydrogenation reaction between physiosorbed CO_2 and H_{ads} ($CO_2 + H_{ads} + e^- \rightarrow HCOO^-$) [57]. The corresponding intermediates were not detected by infrared spectroscopy likely due to low coverage or short surface lifetime of these surface species.

Recently, Dutta *et al.* [58] also used *in situ* Raman spectroscopy to explore the change of the reactive sites of CO_2RR to formate on Bi_2O_3/Bi catalysts as a function of potential. When the potential was > –0.6 V *vs.* RHE, CO_2 intercalation in Bi_2O_3 was observed, forming a "carbonite" species, as suggested by the appearance of Raman peaks at 313 and 162 cm^{-1} which were characteristic fingerprint peaks of Bi oxide and carbonite species, respectively. The author concluded that at low overpotentials (> –0.6 V *vs.* RHE), the carbonite species were converted to format through a coupled proton/electron transfer. However, when the potential was < –0.6 V *vs.* RHE, the Bi oxide/carbonite complex species were reduced, and the metallic state Bi(0) acted as the active site for the reaction. Through *in-situ* infrared spectroscopy and theoretical calculations, Cao *et al.* [55] proposed a new mechanism for the formation of formate on atomically thin bismuthene (Bi-ene) catalysts (Figs. 4(c,d)). In CO_2-saturated 0.5 mol/L $KHCO_3$ solutions at potentials more negative than –1.1 V *vs.* Ag/AgCl, OCHO* species and adsorbed HCO_3^- were formed as indicated by the peaks at 1403 and 1352/1300 cm^{-1} respectively in attenuated total reflection-surface enhanced infrared absorption spectroscopy (ATR-SEIRAS). The authors postulated that OCHO* is a formate intermediate. The downward peak of HCO_3^- indicates that HCO_3^- is consumed. Moreover, the authors also observed the formation of OCHO* and the consumption of adsorbed HCO_3^- in Ar-saturated 0.5 mol/L $KHCO_3$ solution, indicating that HCO_3^- from the solution can adsorb on the electrode and is involved in the reaction in their system. However, it should be pointed out that the peak at 1403 cm^{-1} has also been attributed to carbonate [59], and the peaks at 1352/1300 cm^{-1} are too weak to unambiguously identify. The presence of monodentate OCHO* species remains to be confirmed. A combination of identifying rate-determining steps of CO_2RR, isotopic labeling and theoretical calculation reported by Pérez-Gallent *et al.* [60] is promising in this regard.

3.2. CO_2-to-CO conversion

Au and Ag are recognized as the most selective and active catalysts for the generation of CO due to their weak binding energy to CO [49,61,62]. Theoretical calculations suggest that *COOH adsorbed through the terminal C is an intermediate for the formation of CO [49]. Due to the weak adsorption energy of the intermediate *COOH on Au and Ag, there are some challenges for the analysis of the reaction path. The affinity of CO toward Ag is rather low which makes spectroscopic investigations of mechanistic details much more difficult. Firet *et al.* [63] studied the reaction intermediate and pathway on Ag thin films by means of infrared spectroscopy. In the potential range of –1.4 to –1.6 V *vs.* Ag/AgCl, the peaks at 1288, 1386 and 1660 cm^{-1} were assigned to C–OH, C–O and C=O stretching vibration of the adsorbed *COOH intermediate, respectively. When the overpotential was –1.6 V *vs.* Ag/AgCl, the symmetric and asymmetric stretching vibration peaks of $*COO^-$ with the

C-terminus attached to the Ag surface were found at 1399 and 1559 cm^{-1}. The authors postulated that there are two possible reaction pathways for the CO_2RR on the Ag electrode. In the potential region of –1.4 to –1.55 V *vs.* Ag/AgCl, CO_2 can directly adsorb on the metal surface in the form of *COOH by one-step proton coupled electron transfer. When the pontential is more negative to –1.6 V *vs.* Ag/AgCl, CO_2 can either obtain an electron to form adsorbed $*COO^-$, followed by combination with a proton to generate *COOH, or obtain an electron coupling with a proton to generate *COOH in one step.

Recently, Shan *et al.* [64] used Raman spectroscopy to identify various intermediates of CO_2RR on porous Ag electrodes (Fig. 5(a)). In addition to the observation of C-coordinated *COOH intermediate peaks at 1386 and 1660 cm^{-1}, symmetric (998 cm^{-1}) and asymmetric (1030 cm^{-1}) stretching vibrations of OCO in *COOH were also observed at lower wavenumbers, and peaks at 718, 1130 and 1540 cm^{-1} were attributed to the deprotonated $*COO^-$. Stretching vibrations of O–(CH)–O at 1436 and 1469 cm^{-1} from the *OCHO* intermediate coordinated with two oxygen atoms were also observed. Through isotopic labeling Raman spectroscopy and theoretical calculations, the authors assigned a peak at 408 cm^{-1} to the out-of-plane rocking vibration of Ag–C of *COOH with a top site adsorption configuration, and a peak at 530 cm^{-1} to the OCO out-of-plane wagging vibration of *OCHO* with a bridge site adsorption configuration, respectively. The observation of both *COOH and *OCHO* on the Ag electrode suggest there are two different reaction pathways. The *COOH path forms *CO, which readily desorbs to form gas-phase CO, while in the *OCHO* path, the intermediate is easily reduced to formate.

The rate-determining steps and reaction mechanisms of CO_2RR on Au electrodes have been debated because of the low *CO coverage. Dunwell *et al.* [66] showed that the Tafel slopes obtained on Au and Ag surfaces in the kinetically controlled region (low overpotential) were consistently~59 mV dec^{-1}, suggesting the rate-limiting step is not the initial electron transfer ($CO_2 + e^- \rightarrow CO_2^-$). Wallentine *et al.* [67] developed plasma-enhanced vibrational SFG spectroscopy to observe CO from CO_2RR on Au electrodes. They found that CO coverage was potential dependent suggesting that CO_2 adsorption is the rate-determining step of CO_2RR on Au electrodes.

In recent years, ionic liquids, as a new type of media composed of anions and cations with adjustable acid and base and designable structures, have shown high catalytic activity in CO_2 electroreduction [68]. Much attention has been paid to the mechanism of CO_2 conversion to CO. García Rey *et al.* [69] found that in 1-ethyl-3-methylimidazolium tetrafluoroborate (EMIM-BF_4) containing 0.3 mol% water, the FE of CO was close to 100% for CO_2 reduction on polycrystalline Ag electrodes at low overpotentials. SFG showed that CO did not poison the Ag surface during CO_2RR, which helps to prolong the life of the CO_2 reactor. The electrochemically driven ionic liquid structure transition within the double layer enables enhanced electric field strength to control CO_2 reduction, as reflected in the stark slope of adsorbed CO shift from 24 to 55 cm^{-1} V^{-1} at potentials negative of –1.33 V *vs.* Ag/AgCl. Rosen *et al.* [70] used EMIM-BF_4 with 90 mmol/L water as the electrolyte and

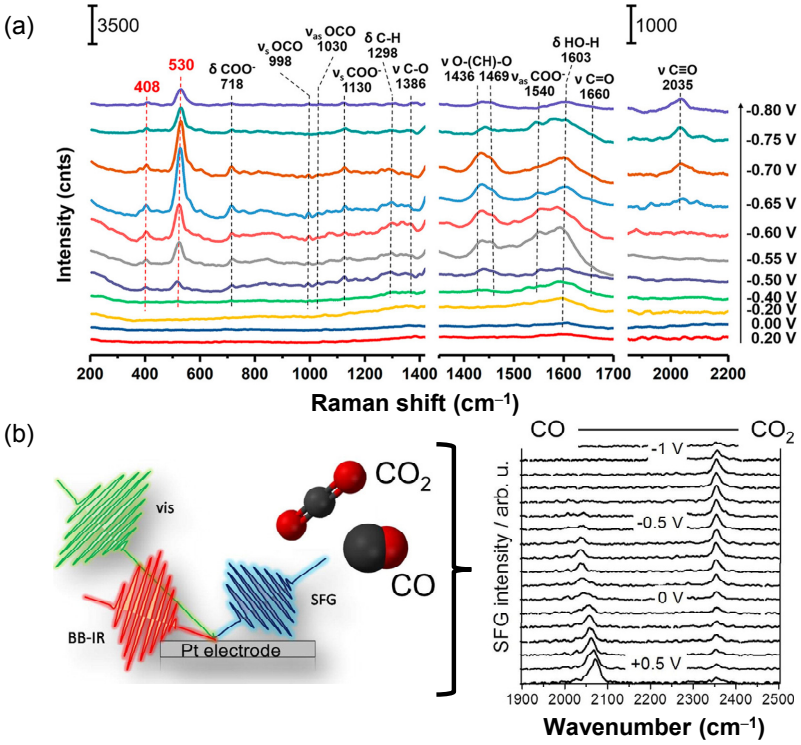

Fig. 5. (a) *In situ* SERS spectra of CO_2RR at nanoporous Ag surfaces in 0.1 mol/L $KHCO_3$ solution saturated with CO_2. The arrow on the right shows the potential scanning direction. Peaks marked with black and red dashed lines are attributed to the reported and new SERS signals, respectively. Reprinted with permission from Ref. [64]. Copyright 2020, American Chemical Society. (b) Vibrational sum-frequency generation study of CO_2RR at Pt/EMIM-BF_4 interfaces. Reprinted with permission from Ref. [65]. Copyright 2016, Elsevier.

co-catalyst and were able to obtain adsorbed CO at –0.25 V *vs.* SHE on Pt electrodes during CO_2RR. They observed a peak at 2348 cm^{-1} in the electrochemical SFG spectra and attributed it to a $[EMIM\text{-}CO_2]_{ad}$ complex intermediate formed on the electrode surface during the electrolysis process. The authors ruled out the possibility of this peak arising from dissolved CO_2 on the basis of SFG selection rules. Dissolved CO_2 has an inversion symmetry and therefore is not SFG active. The formation of this adsorbed complex reduced the CO_2 activation energy barrier and the reduction overpotential. In addition, the $[EMIM]^+$ layer on the electrode surface suppressed the formation of H_2 and thus enhanced CO_2 coversion. Braunschweig *et al.* [65] also found a stable $[EMIM\text{-}CO_2]$ intermediate (2355 cm^{-1}) at Pt electrodes during CO_2 reduction with SFG spectroscopy (Fig. 5(b)). They postulated that CO_2 molecules confined at the Pt-$[EMIM]BF_4$ interfaces are very different from gaseous CO_2 or dissolved CO_2.The authors found that CO linearly bonded to Pt is the predominant surface species for CO_2RR product. The accumulation of CO during CO_2RR leads to a considerable poisoning effect which causes a massive drop in current densities after several potential cycles.

3.3. CO_2 Reduction to CH_4 and C_{2+} products

Cu is the only catalyst capable of converting CO_2 to an appreciable amount of multi-carbon products. A large number of theoretical calculations have been reported on the reaction mechanism of CO_2RR on Cu [17], but solid experimental evidence remains sparse. It is generally accepted that adsorbed CO generated by CO_2 electroreduction is a key intermediate for the subsequent generation of C_1 or C_{2+} products [4,18,71]. For the reaction path of generating CH_4, *CHO is generally considered a key intermediate, and the reaction invovles multiple proton and electron transfer steps [4]. For C_{2+} products, there are two possible paths, one is that $*CH_2$ is coupled to generate C_2H_4, and $*CH_3$ is coupled to generate C_2H_6; the other is *CO dimerization to generate *OCCO* intermediate, further coupled with proton and electron to form ethylene or ethanol [18].

Pérez-Gallent *et al.* [60] provided spectroscopic evidence for the reaction intermediate of CO reduction (CORR) to C_{2+} product. Using *in situ* external reflection IR spectroscopy and isotopic labeling, peaks at 1191 and 1584 cm^{-1} were observed on Cu(100) electrodes in CO-saturated LiOH solution in H_2O and D_2O, respectively. Based on the the theoretical calculations (Fig. 6(a)), the authors attributed the two peaks to the stretching vibrations of C–O–H and C–O of the hydrogenated dimer (OCCOH), providing direct spectroscopic evidence for *CO dimerization. However, under exactly the same conditions, no hydrogenated dimer peak was observed on Cu(111)

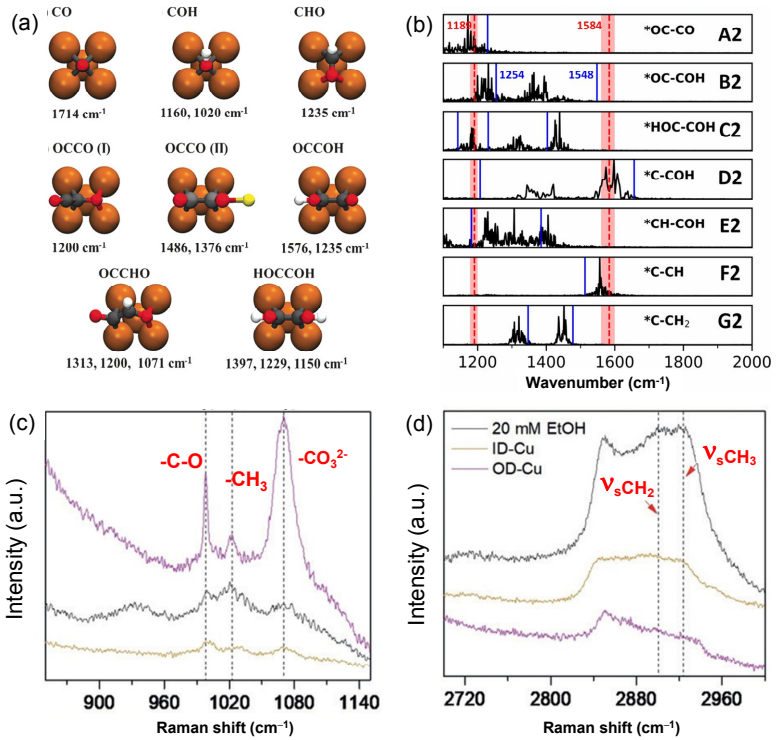

Fig. 6. (a) Simulated structures of possible adsorbates on Cu(100) for CO_2RR and their calculated infrared-active vibrational frequencies. Cu, Li, C, O, and H atoms are depicted as orange, yellow, gray, red and white spheres. Reprinted with permission from Ref. [60]. Copyright 2017, John Wiley and Sons. (b) The vibrational density of states (*v*-DoSs) of *OC–CO, *OC–COH, *HOC–COH, *C–COH, *CH–COH, *C–CH, *C–CH_2, and *C=C=O intermediate. In A2-G2, *v*-DoS from quantum mechanics molecular dynamics (QM-MD) is shown as a solid black line, the experimental frequencies are shown as a red dashed line, and the vibrational frequencies from *v*-QM optimization are shown as solid blue lines for comparison. Reprinted with permission from Ref. [51]. Copyright 2019, Proceedings of the National Academy of Sciences. (c) *In situ* Raman spectra in CO_2-saturated 0.2 mol/L $NaHCO_3$ for iodide-derived copper (ID-Cu) and oxide-derived copper (OD-Cu) samples shown the enlarged region between 850–1150 cm^{-1} at –1.0 V *vs.* Ag/AgCl and (d) The $-CH_x$ stretching region between 2700–3000 cm^{-1} at –0.8 V *vs.* Ag/AgCl. Reprinted with permission from Ref. [72]. Copyright 2020, John Wiley and Sons.

electrodes, suggesting that the dimerization of *CO depends on the Cu structure. Cheng *et al*. [51] recently used molecular dynamics simulations to predict the spectral peak positions of possible products of CO_2RR taking careful consideration of actual reaction conditions such as solvent, electrode-electrolyte interface, temperature, and potential (Fig. 6(b)). Instead, the C–O stretching vibration of *HOC–COH and the C–C stretching vibration of *C–COD, rather than the previsouly suggested ν(C–O–H) and ν(C–O) modes of *OCCOH, were assigned to the peaks observed by Koper *et al*. [60]. More advanced simulations with careful isotope labeling are needed to resolve this disagreement.

Recently, Kim *et al*. [73] simultaneously observed the intermediates of CO_2RR reduction to methane and ethylene on Cu, using time-resolved ATR-SEIRAS. The authors constructed two types of Cu electrodes, a $Cu(OH)_2$-derived Cu catalyst (P-Cu), on which the CO_2RR formed mainly C_{2+} products. The other is the electrodeposited Cu thin film (ED-Cu), and the main product was methane. Using theoretical calculations and isotopic substitutions, the authors attributed the observed peaks at 1550–1562 and 1760 cm^{-1} to *OCCO for ethylene and *CHO for methane, respectively. *OCCO was observed on the P-Cu catalyst while *CHO not. The authors deduced that ethylene was formed through CO dimerization to *OCCO, without involving *CHO. Methane, on the other hand, was generated by the *CHO pathway through CO hydrogenation. The C–C coupling mechanism on different Cu-based catalysts may be different. Ma *et al*. [74] observed *CHO (1754 cm^{-1}) on fluorine-modified copper (F-Cu) catalyst, and proposed a H-assisted C–C coupling mechanism, where CO hydrogenation generates *CHO, which is then coupled to form *OCHCHO*. The F-Cu catalyst exhibited high C_{2+} product selectivity, and the authors proposed that the *CHO species plays an important role in the C–C coupling of the F-Cu catalyst. Interestingly, Li *et al*. [75] demonstrated that the rate-determining step of CORR to C_{2+} products, besides CO dimerization, may also be affected by hydrogenation of CO with H_2O as a proton source through *in situ* infrared, Raman spectroscopy and electrokinetic investigations. The rate-determining step for methane production is related to the pH of the electrolyte, which is limited by the CO hydrogenation *via* proton coupled electron transfer in weak alkaline conditions (7 < pH < 11) or CO chemical hydrogenation *via* adsorbed hydrogen atoms in strong alkaline electrolyte (pH > 11).

The reaction pathways for ethylene or ethanol formation generally follow the dimerization of *CO pathway despite some modifications [4], while there is less spectroscopic evidence for the reaction pathway for ethane. There are two possible reaction pathways to ethane [72,76–79]: (1) hydrogenation of the pre-formed ethylene; (2) direct coupling of two $*CH_3$ intermediates. Vasileff *et al*. [72] found that iodide-derived Cu (ID-Cu) can convert CO_2 to ethane with high selectivity. They attributed this observation to that ID-Cu has an optimized Cu oxidation state, which may improve the stability of O-binding species and facilitate the hydrogenation of hydrocarbons to ethane. Their experimental results showed that the reaction paths of ethane, ethylene and ethanol were the same. They all undergo *CO coupling to generate C–C bonds instead of $*CH_3$ coupling. Further support of this assertion comes from the observed Raman spectra of the symmetric stretching vibrations of $–CH_2$ and $–CH_3$ at ~2890 and~2920 cm^{-1} of oxygen-bound ethoxy ($*OCH_2CH_3$) on ID-Cu which is an intermediate of ethane formation (Figs. 6(c,d)). Huang-Fu *et al*. [80] reported that on Cu electrodes, C–H stretching vibration peaks corresponding to surface-adsorbed ethoxy intermediate ($Cu\text{-}OCH_2CH_3$) at –0.7 V *vs*. SCE were observed by SFG spectroscopy, which may be the surface intermediate species for the generation of ethanol.

4. The role of CO in CO_2RR

CO plays an important role in CO_2RR. Besides being a key intermediate for gas-phase CO, CH_4 and C_{2+} products, its adsorption configuration and coverage also affect the selectivity and activity of CO_2RR. CO can also be used as a molecular probe to indirectly obtain catalyst surface structures. There are two main adsorption configurations of CO on the metal electrode related to CO_2RR: the linearly bonded CO (CO_{top}) where CO binds to one metal atom and the bridge-bonded CO (CO_{bridge}) where CO interacts with two or three metal atoms (here we do not intend to separate the bridge and hollow adsorption sites) [81]. The roles of the two CO adsorption configurations in CO_2RR are still controversial. Some studies suggested that CO_{bridge} is inert, and acts only as a spectator that does not participate in CO_2RR due to CO_{bridge} stablized by the interfacial electric field [82]. Others showed that CO_{bridge} is reactive with the assistance of CO_{top} [83]. To address this issue, researchers used vibrational spectroscopy to explore the role of CO with different adsorption configurations, and found that the adsorption configuration of CO depends on the electrode, coadsorbate and solution pH [81]. In this section, we discuss the effects of CO adsorption configuration and coverage on CO_2RR, and the use of CO as a molecular probe in CO_2RR.

4.1. CO adsorption configuration

It has been well documented that the C≡O stretching peak for the CO_{top} is located at 2130–2000 cm^{-1}; and for the CO_{bridge}, it is at 2000–1650 cm^{-1} [81], as shown in Fig. 7. The adsorption configuration and adsorption strength of CO on a metal depend on the electronic structure of the metal. In CO_2RR, although CO is a key intermediate, the role of CO_{bridge} and CO_{top} is different.

Using *in-situ* ATR-SEIRAS, Wutting *et al*. [84] found that the surface population of electrogenerated CO_{bridge} is much higher than CO_{top} on Au electrodes under the condition of CO_2RR. However, CO_{top} was an active intermediate of CO_2RR on Au electrodes to generate gas-phase CO, while CO_{bridge} was irreversibly adsorbed and could only be removed by positive potential oxidation (Fig. 8(a)). Jiang *et al*. [85] found that the adsorption of CO_{bridge} on Pd electrodes is much stronger than that of CO_{top}. However, at higher overpotentials, CO_{top} is an active intermediate to generate gas-phase CO, while CO_{bridge} acts as a bystander and does not participate in the reaction (Fig. 8(b)). Gunathunge *et al*. [82] clarified the roles of CO_{top} and

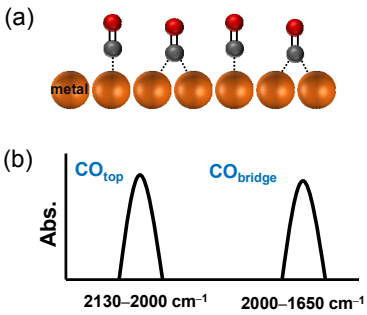

Fig. 7. The adsorption configuration of CO on metal electrodes and the corresponding positions in the vibrational spectrum.

CO_{brigde} species on Cu electrodes during CORR with the aid of *in situ* ATR-SEIRAS. In CO-saturated 0.05 mol/L Li_2CO_3 solution, when the potential was scanned from positive to negative, CO_{top} and CO_{brigde} appeared at the same potential (~–0.6 V *vs.* SHE) and the integrated intensity for both bands increased. During the reverse potential scan, the decline of the CO_{top} band intensity was highly reversible while the intensity change of the CO_{bridge} exhibited a ramarkable degree of hysteresis. When the CO-saturated solution was purged by Ar, the surface-adsorbed CO_{top} intensity decreased while the CO_{brigde} intensity monotonic increased at –1.1 V *vs.* SHE. When the potential was stepped to –1.75 V *vs.* SHE, the CO_{brigde} band intensity remained largely unchanged while the CO_{top} band disappeared. DFT calculations revealed that the hydrogenation of CO_{bridge} to *CHO (active intermediate for CH_4 formation) on Cu(100) needs to climb a higher energy barrier than CO_{top}. The authors further speculated that a part of CO_{top} may be converted into CO_{bridge}, and CO_{top} is the reaction intermediate to produce multicarbon products instead of CO_{bridge} (Fig. 8(c)). In addition, CO_{brigde} is more likely to appear on the Cu electrode under strong alkaline conditions or potential-induced surface reconstruction [82]. Recently studies [86] reported that the CO adsorption configuration depends on the valence state of Cu under CO_2RR conditions (Fig. 8(d)), and CO_{brigde} is reactive when it coexists with CO_{top}. *In situ* ATR-SEIRA spectra showed that on Cu electrodes with Cu(I), there was only CO_{top} peak, and the product was mainly methane; while on Cu electrode with Cu(0), there was only CO_{bridge} peak, and the product was mainly H_2. Interestingly, both CO_{top} and CO_{brigde} were observed on Cu electrode with both Cu(I) and Cu(0), and their co-existence enhanced the CO_2 to ethylene selectivity. A surface Raman spectrocopic report by Chang *et al.* [87] further confirmed that the CO adsorption configuration is related to the pH of the electrolyte and surface composition at Cu electrode.

Recently, Li *et al.* [83] found that the selectivity of ethylene is related to the ratio of CO adsorption configuration (CO_{top}/CO_{brigde}) on tetrahydro-bipyridine modified Cu electrodes using Raman spectroscopy during CO_2RR. The experimental results showed that when the CO_{top}/CO_{brigde} ratio is between 0.4–0.5, the FE of ethylene can reach more than 60%. Theoretical calculations further indicated that the dimerization between CO_{top} and CO_{bridge} on Cu(111) has the lowest energy barrier, suggesting that high ethylene selectivity comes from the right amount of CO_{top} and CO_{bridge}.

4.2. *CO coverage effect*

Adsorbed CO is a key intermediate of hydrocarbons, oxygenates and CO gas for CO_2RR processes, hence the CO coverage may modulate the product selectivity. Zhan *et al.* [88] used *in situ* Raman spectroscopy to establish the correlation of C_{2+} product selectivity and potential-dependent CO surface coverage on Cu_2O nanocubes under CO_2 reduction conditions. Cu-CO rotation (P1, ~280 cm^{-1}), Cu-CO stretching vibration (P2, ~355–370 cm^{-1}) and C–O stretching vibration (~1970–2110 cm^{-1}) were observed in the Raman spectra. The authors used the intensity ratio of the two peaks P2/P1 to represent the potential dependent CO coverage. As the

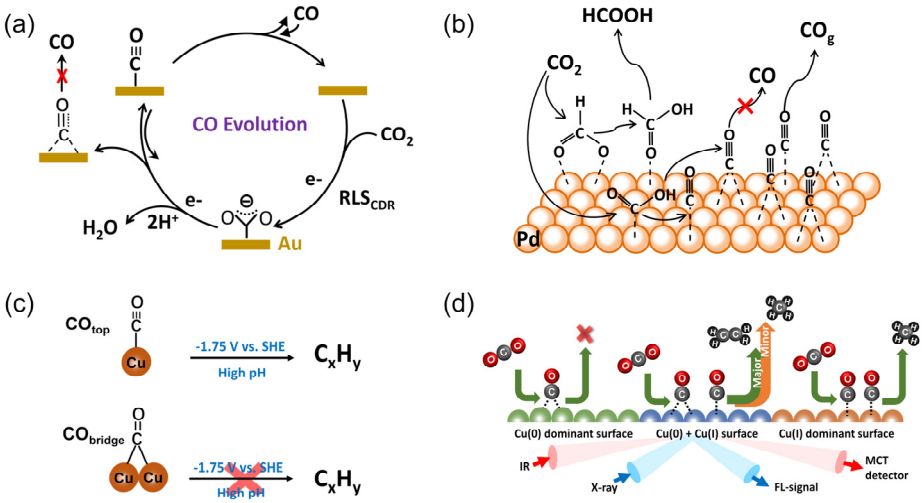

Fig. 8. The schematic diagrams showing the roles of CO_{top} and CO_{brigde} on different electrodes. (a) Au electrode. Reprinted with permission from Ref. [84]. Copyright 2016, Proceedings of the National Academy of Sciences. (b) Pd electrode. Reprinted with permission from Ref. [85]. Copyright 2021, American Chemical Society. (c) polycrystalline Cu electrode. Reprinted with permission from Ref. [82]. Copyright 2018, American Chemical Society. (d) Cu electrode with Cu(0) and Cu(I). Reprinted with permission from Ref. [86]. Copyright 2020, American Chemical Society.

potential was negatively shifted from –0.6 to –0.9 V *vs*. RHE, the P2/P1 value increased from 0.7 to 1.4, and reached a maximum value at –1.0 V, then decreased rapidly, showing a volcano-shape trend. This spectral result is consistent with a previous report [89]. The P2/P1 ratio or CO coverage is correlated with the FE of C_{2+} products, in which a low CO coverage is unfavorable for CO_2 to C_2H_4 conversion. Gunathunge *et al*. [90] reported that at a sufficiently high CO coverage the interaction of CO with Cu may induce the reconstruction of the Cu surface to form Cu clusters containing unsaturated sites, changing the product selectivity. The modification of Cu with N-doped C (N_xC) could enrich and activate interfacial CO_2 *via* the specific N-CO_2 interaction, and the resultant higher CO coverage as monitored by IR spectroscopy may promote the selective C_{2+} formation on Cu [91]. Recently, Wuttig *et al*. [92] revealed that competitive adsorption of water and anion affects CO coverage *via* a combined *in situ* infrared spectroscopy and voltammetry approach. Reversible CO binding to Au competes with adsorbed water, and the adsorption of water can release CO_{ads} from Au catalysts, hindering its further reduction. In contrast, CO binding to Cu requires the reductive displacement of adsorbed carbonate anions. At negative potentials, carbonate desorption facilitates CO accumulation on Cu, allowing its further reduction to multicarbon products.

Notably, in a specially designed experiment with CO adsorption and reduction under controlled stirring, Malkani *et al*. [93] reported that increasing the mass transport increases the overall coverage of CO on Cu electrode, and yet the CORR product selectivity seems not to be changed significantly. The authors assigned the peculiar result to the random distribution of adsorbed CO.

4.3. CO as a surface probe

Since C≡O stretching vibration frequency is very sensitive to the CO adsorption environment, CO can be used as a molecular probe to monitor the surface structure of a CO_2RR catalyst. For example, the C–O stretching band (ν_{CO}) from CO adsorbed on the defect sites of Cu is located in the high frequency region (~2080 cm^{-1}) [94], where it is in the lower frequency region (~2040 cm^{-1}) for CO adsorbed on the terrace sites [94]. CO on Cu^+ sites has a ν_{CO} band above 2100 cm^{-1} [95–97], while that on Cu^0 sites is located at ~2050–2070 cm^{-1} [96,97].

Gunathunge *et al*. [94] identified atomic-scale surface structures on two commonly used Cu thin films for CO_2RR by infrared spectroscopy using CO as the probe. Two Cu thin films with dominant Cu(111) and Cu(100) planes were prepared by electrochemical deposition and chemical deposition, respectively. On the electrodeposited Cu film, the C–O stretching peak is in the high frequency region (2080 cm^{-1}); on the chemically deposited Cu film, C–O stretching band appears in both the low frequency region (2045 cm^{-1}) and the high frequency region (2080 cm^{-1}). These observations suggest that the chemically deposited Cu films have various adsorption sites such as defects and terraces, while the electrodeposited Cu films consist of more defect sites.

An *et al*. [98] employed sub-second time-resolved Raman spectroscopy to identify Cu electrode surface reconstruction by CO molecules, and correlated CO adsorption sites on Cu with CO_2RR product selectivity. The authors found that on anodically oxidized Cu electrodes, different reduction potentials yielded different surface structures and different products (Fig. 9). When the potentail was stepped to –0.7 from +1.55 V *vs*. RHE in CO_2-saturated 0.1 mol/L $KHCO_3$, a CO peak appeared at 2058 cm^{-1} within 2 s and redshifted in the first 7 s before blueshifted to 2092 cm^{-1} in ca. 12 s. The lower frequency band was assigned to CO adsorbed on terrace-like sites and the higher frequency band to CO on isolated defect-like sites. Together with the chronoamperometric results and Raman spectra at lower wavenumber region, the observed spectral transitions were explained in terms of redeposition of dissolved copper species, and the main CO adsoprtion site changes from terrace-like to defect-like sites induced by more dominat OH adsoprtion due to decreasing local pH caused by hydrogen evolution reaction. The authors argued that the CO intermediates on isolated defect-like sites can not couple to form CO–CO dimer, hence the main CO_2 reduction product at –0.7 V *vs*. RHE is CO. Given that CO adsorption on defect sites is stronger than on the terrace sites, it is intriguing that CO adsobed on terrace sites appeared first. When the potential was stepped from +1.55 to –0.9 V *vs*. RHE, the spectra in the C–O stretching region were dominant by a band at aournd 2050 cm^{-1} that was assigned to CO adsorbed on step-edge defect sites, which are similar to CO adsorbed on terrace sites. These

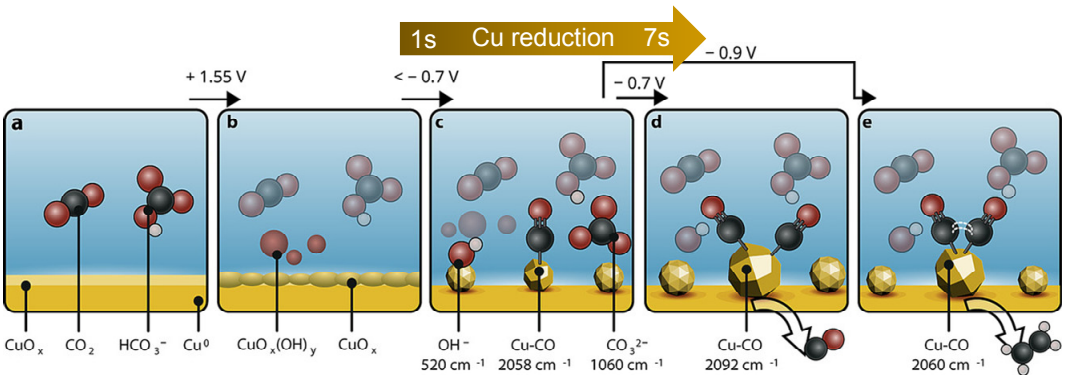

Fig. 9. Schematic diagrams for the observed processes on anodic treatment of mechanically polished polycrystalline Cu electrode during CO_2RR using *in situ* time-resolved surface-enhanced Raman spectroscopy. Reprinted with permission from Ref. [98]. Copyright 2021, John Wiley and Sons.

CO can be further coupled to generate C_{2+} products such as ethylene. These results illustrate that CO dimerization is related to its adsorption site and the applied reduction potential.

Malkani *et al.* [97] used CO adsorption to identify the Cu surface structure by infrared spectroscopy under alkaline conditions. They observed three peaks at 2131, 2089, and 2073 cm^{-1} for CO adsorption on polycrystalline Cu electrodes. Traditionally, the peak at 2131 cm^{-1} was assigned to CO adsorbed on Cu^+. However, as argued by the authors, metallic Cu could not be oxidized to Cu_2O at –0.4 V *vs.* RHE. In addition, no CO peak at 2131 cm^{-1} was observed on an intentionally constructed CuO_x surface or Au film. Thus, the authors proposed that the peak at 2131 cm^{-1} is from CO adsorbed on reconstructed Cu sites instead of Cu^+ sites.

5. Influence of electrode structure and composition on CO_2RR

There have been numerous reports that CO_2RR selectivity and activity depend on the catalyst structure and composition. However, identifying active sites of a catalyst with an aim to improve its catalytic performance remains challenging. Among others, it is debatable what the active sites are for oxide-derived Cu-based catalysts, Cu-based bimetallic catalysts and non-metal doped Cu catalysts. This section summarizes the key findings in recent literature on the fundamental understanding of the composition and structure effects of electrocatalytic materials on CO_2RR performance.

5.1. Oxide-derived Cu-based catalysts (OD-Cu)

Since Kanan and coworkers [99] developed the OD-Cu catalyst to facilitate the conversion of CO_2 to C_{2+} products, more and more efforts have been devoted to the construction of Cu electrodes containing oxide species [100–102]. However, it has been questioned whether surface oxide species such as (CuO_x, $CuO_x(OH)_y$) can exist stably under CO_2RR conditions [87]. Some studies suggest that $Cu^{\delta+}$ is the active site of the catalyst on oxide-derived Cu [103–106], but others argued that the defect sites, grain boundaries and crystal planes formed after rapid reduction of the surface oxidized Cu may be the active sites [101,107–110].

5.1.1. Oxidation state of Cu

Interestingly, it has been proposed that under CO_2RR conditions, slightly positively charged $Cu^{\delta+}$ on the Cu surfaces is the active site for the formation of C_{2+} products [100,103,112]. Patra *et al.* [111] found that B-doped CuO can stabilize the $Cu^{\delta+}$ species and enhance the C_{2+} product selectivity. Three C–O stretching peaks at 2050, 2072 and 2080 cm^{-1} were observed on B-CuO electrode during CO_2RR by ATR-SEIRAS, suggesting that there are various active sites on the Cu surface, of which 2080 cm^{-1} belongs to CO adsorption on low-coordinated sites on the $Cu^{\delta+}$ surface (Fig. 10(a)). However, only 2050 cm^{-1} was observed on CuO-derived Cu electrode, which arises from CO adsorbed on the metallic Cu sites. The blue shift of the C-O stretching frequency of CO adsorbed on B-CuO-derived Cu electrode with respect to that on CuO-derived Cu electrode was attributed to the change of oxidation state caused by the charge transfer between B and Cu. The intensity of the $Cu^{\delta+}$ related CO band at 2072–2080 cm^{-1} increased with the increasing overpotential which the authors attributed to the stronger adsorption of *CO on the $Cu^{\delta+}$ active site that leads to a higher CO coverage. They concluded that multiple CO adsorption sites

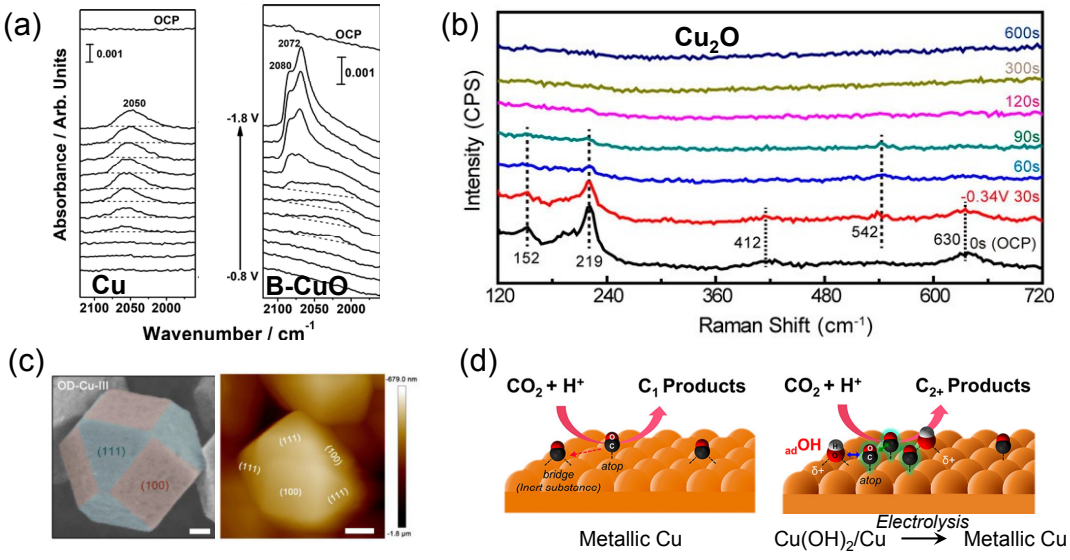

Fig. 10. Controversial views on OD-Cu catalysts during CO_2RR. (a) Partially positive-charged copper ($Cu^{\delta+}$) is to boost the formation of highly valued multicarbon C_{2+} products during CO_2RR. Reprinted with permission from Ref. [111]. Copyright 2020, American Chemical Society. (b) The electrochemical prereduction process, during which Cu_2O nanocubes were converted into metallic Cu phase under a negative potential of –0.34 V *vs.* RHE. Reprinted with permission from Ref. [32]. Copyright 2020, Proceedings of the National Academy of Sciences. (c) Cu(100)/Cu(111) interfaces as superior active sites for CO dimerization during CO_2RR. Reprinted with permission from Ref. [109]. Copyright 2021, American Chemical Society. (d) Role of a hydroxide layer on Cu electrodes in electrochemical CO_2 Reduction. Reprinted with permission from Ref. [95]. Copyright 2019, American Chemical Society.

(Cu^0 and $Cu^{\delta+}$) and higher CO binding energy on $Cu^{\delta+}$ facilitate the CO dimerization which improves the C_{2+} product selectivity. It should be mentioned that linking the C–O vibrational band at 2072–2080 cm^{-1} to the $Cu^{\delta+}$-CO is not a concensus, in fact, such a species has been referred to the band above 2100 cm^{-1} [97] and the observed band at ca. 2080 cm^{-1} may be also attributable to CO adsorption on Cu defect sites [94]. Iijima *et al*. [96] found that methyl thiol desorption induced surface reconstruction and Cu^+ formation at high overpotentials on methyl thiol-modified Cu (MT-Cu) electrodes. Infrared spectroscopy showed that on the MT-Cu electrode, the CO peak broadened and shifted to higher wavenumbers at ca. 2100 cm^{-1}. The authors postulated that the Cu surface reconstruction forms a variety of CO adsorption sites, and the presence of Cu^+ improves the selectivity of CO_2RR to ethylene. Recently Yang *et al*. [113] synthesized a Cu_2O catalyst with porous structure that enables the efficient confinement of carbon-related intermediates including *CO, a high CO coverage on the surface slows down the reduction of Cu^+ to Cu(0). Moreover, such confined intermediates also promote C–C coupling inside the reactive nanocavities, giving rise to the high C_{2+} selectivity.

5.1.2. Grain boundaries/crystal plane

Hori *et al*. [48] found that the product of CO_2RR highly depends on the Cu crystal orientation. Among them, Cu(100) is beneficial to reduce the energy barrier of CO dimerization with ethylene being the main product, while Cu(111) is energetically unfavorable for CO dimerization with methane being the main product. More interestingly, the grain boundaries formed between different crystal planes have been shown to improve the product C_{2+} selectivity due to the changes of the local atomic arrangement and electronic structure [107,114,115]. Along this line, the grain boundaries or new crystal planes formed on oxide-derived Cu-based catalysts during the reduction process were suggested to be responsible for the enhanced C_{2+} product selectivity [107,116,117].

Zhu *et al*. [32] used time-resolved Raman spectroscopy to study the surface state changes of Cu_2O nanocrystals with (100) orientation during CO reduction reaction (Fig. 10(b)) in the context to simplify the study of CO_2RR. At open circuit potential, Raman peaks characteristic of Cu_2O nanocrystals were detected at 152, 219, 412, 542 and 630 cm^{-1}, with the one at 219 cm^{-1} as the main peak. Upon applying –0.34 V *vs*. RHE during CORR, the peak intensity of the oxide gradually decreased and disappeared suggestive of the formation of metallic Cu. In combination with DFT calculations, the authors suggested that the coupling of Cu(100) terrace sites with adjacent step sites along the edge contributes to the selective production of acetic acid. Malkani *et al*. [97] probed the change of oxidation state of OD-Cu during CO electroreduction under alkaline conditions by infrared spectroscopy. An additional peak at 2058 cm^{-1} was observed, which is close to the peak position of CO adsorption on Cu(100). This observation suggests that there are exposed Cu(100) facets on OD-Cu. The authors proposed that the preferential adsorption of CO on exposed Cu (100) surface of OD-Cu is the key reason for the increase of C_{2+} product selectivity on OD-Cu. Similar conclusions have been drawn in other related studies on Cu electrodes of different surface morphologies and crystallographic orientations [88,118].

Recently, Wu *et al*. [109] prepared Cu_2O nanocrystals with controllable crystal facets, and obtained a series of Cu nanocrystals with adjustable ratios of Cu(100) and Cu(111) crystal facets after electroreduction, which improved the C_{2+} product selectivity. *In situ* IR and Raman spectroscopies and theoretical calculations show that the Cu(100)/Cu(111) interface has an optimal electronic structure that enhances *CO adsorption and lowers the activation energy barrier for CO–CO dimerization (Fig. 10(c)). Zhong *et al*. [108] found that for $Cu(OH)_2$-derived Cu catalysts all of the characteristic Raman bands associated with $Cu(OH)_2$, CuO and Cu_2O disappear after polarization at –0.5 V *vs*. RHE in CO_2-saturated 0.1 mol/L $KHCO_3$ aqueous solution for several minutes. These results demonstrate that $Cu(OH)_2$-derived/Cu is reduced to metallic copper during CO_2RR. The $Cu(OH)_2$-derived Cu catalysts expose relatively high density of stepped Cu(110) and Cu(100), which are assembled into Cu(210) and Cu(310), promoting CO adsorption and CO dimerization and leading to improved CO_2RR catalytic activity to C_{2+} products.

5.1.3. Hydroxide species

For oxide-derived Cu-based catalysts, recent studies have also found that the surface hydroxide species can play a role in the catalytic activity [95,119]. Iijim *et al*. [95] found that on $Cu(OH)_2$/Cu electrodes, OH residing on the Cu surface plays an important role in CO_2RR and the formation of C_{2+} products. It was confirmed by infrared spectroscopy and isotopic labeling that although Cu^{2+} or $Cu(OH)_2$ was reduced at negative potentials, the surface OH or OD species (2700 cm^{-1}) always existed, occupying the bridge and hollow sites on Cu, hindering the CO_{bridge} adsorption (Fig. 10(d)). The coupling of the adsorbed OH with the CO_{top} may improve C_{2+} selectivity. Recently, He *et al*. [119] added oxygen or hydrogen peroxide to the CO_2RR system to form a stable surface hydroxyl group on Cu surfaces, which significantly increased the partial current density of C_{2+} products at certain potentials, and the onset potential of methane generation also shifted 200 mV positively. Theoretical calculations show that the presence of OH reduces the activation Gibbs free energy of the rate-determining step for generating multicarbon products and methane. Enhanced rate of CO_2RR reduction to CO was also observed on Ag electrodes where surface O_xH_y speceis were detected [120]. Deng *et al*. [121] pointed out that the OH species on Sn surfaces promoted the CO_2 adsorption and enhanced the CO_2RR to HCOOH selectivity.

5.2. Cu-based bimetallic catalysts

The selectivity for a specific product of CO_2RR is not high on monometallic Cu electrode. Construction of Cu-based bimetallic catalysts by means of surface modification or alloying with another metal has attracted considerable interests. For instance, an increased selectivity towards ethylene production was attained on Ag decorated Cu catalysts [122–126], CuAg

alloy [127–129], and oxide-derived CuZn [130]. Studies suggested that the CO generated on Ag overflows to the surrounding Cu atoms, and is further utilized by the Cu atoms to generate multi-carbon products [131–133]. Recently, Herzog *et al*. [126] constructed Ag-modified Cu_2O nanocrystals (Ag/Cu_2O) and explored the synergistic mechanism of Ag and Cu. The reduction of Cu_2O species and the adsorption of CO during the reaction were monitored by *in situ* Raman spectroscopy. The rotational and stretching vibrational peaks of Cu-CO (at 280 and 366 cm^{-1}) were observed on both Ag/Cu_2O and Cu_2O catalysts. On Cu_2O, the peak intensity of the rotational and stretching vibrations of Cu-CO were similar. However, the intensity of the stretching vibration of Cu-CO on Ag/Cu_2O is much stronger than that of the rotational vibration, indicating that the multiple sites constructed by Ag modification constrain the rotational vibration. In addition, the stretching vibration peak intensity of Cu-CO on Ag/Cu_2O decreases with the negative shift of potential, indicating the consumption of CO, which also reflects that the stretching vibrational mode enhances the C–C coupling of adjacent CO molecules on Cu, thereby promoting the C_{2+} products. In a similar work, Li *et al*. [129] found that in Raman spectra the CO peaks from CO on Ag/Cu alloy catalysts were wider than those on pristine Cu, indicating that the modified catalysts have multiple reaction sites and multiple adsorbed intermediates.

Notably, despite the fact that Cu, Ag and Au are in the same IB group, Cu is markedly different from Ag and Au in terms of CO_2RR product distribution given that the latter two produce CO predominantly. In pursuit of an exclusive CO evolution on Cu-based electrodes, atomically deposited Pd layer over Cu foil was reported to enhance CO_2-to-CO conversion [134]. The *in situ* infrared spectroscopy results show that the IR band corresponding to adsorbed CO appears 300 mV more positive on CuPd than that on pure Cu, indicating a more favorable CO formation kinetics at the presence of Pd decoration. A predominant CO_2RR to CO formation was reported on a Sb-modified Cu electrodes (Sb-Cu) [135]. Electrochemical ATR-SEIRAS detected a relatively weak and redshifted CO band on Sb-Cu electrode as compared to that on Cu electrodes at CO_2RR potentials. DFT calculations revealed that Sb clusters on the Cu surface change the electronic structures of Cu and adjacent Sb and thus weaken the CO binding strength on Cu sites, consistent with the observed CO band feature and high CO selectivity.

5.3. Nonmetal doping

Nonmetal doping may also cause the structrural modification on a catalyst, which may affect the surface chemical properties of the catalyst and thus the activity and selectivity of CO_2RR [136–138]. It has been demostrated that S-doped or modified Cu-based catalysts selectively converted CO_2 to formate [57,139–141]. Using *in situ* infrared spectroscopy, Phillips *et al*. [57] reported that the adsorption strength of CO on S-doped Cu (SD-Cu) electrode was enhanced with negative shift of potential, which inhibited the formation of $HCOO_{ads}$ but promoted the direct reaction of CO_2 with the adsorbed hydrogen coupled with electron transfer to form formate. Deng *et al*. [139] applied *in situ* Raman spectroscopy to further explore the CO_2 electroreduction process on the Active-CuS*x* electrode. Contrary to Phillips's work, the authors did not observe the adsorbed CO (2080 cm^{-1}), and they proposed that S inhibited the adsorption of CO on Cu. In addition, the formate precursors $HCOO_{ads}$ (2890 cm^{-1}) and $DCOO_{ads}$ (2140 cm^{-1}) were detected on the bare Cu electrode, but not on the Active-CuS_x electrode, which the authors attributed to the high $HCOO^-$ conversion rate. Recently, Pan *et al*. [140] used the same approach to study the intermediate HCOO* for the conversion of CO_2 to formate on S-doped Cu, and argued that the doping of S enhanced the adsorption of carbonate intermediate during CO_2 electrolysis.

The Cu^+ sites on the Cu surface are considered as the active sites to selective CO_2RR. However, Cu^+ is unstable at negative potential, and the doping of B can stabilize Cu^+. Recently, Zhou *et al*. [103] first reported that B-doped Cu catalysts can improve C_{2+} product selectivity. They used $NaBH_4$ as the B source and obtained Cu-B catalysts with different atomic ratios of Cu/B by adjusting the amount of the Cu precursor. Theoretical calculations and *in situ* X-ray near-edge absorption spectroscopy (XANES) confirmed that B stably exists in the subsurface of Cu and modulates the electronic structure of Cu, keeping Cu in the $Cu^{\delta+}$ valence state. The content of $Cu^{\delta+}$ increases with increasing B concentration. The doping of B inhibits the conversion of CO_2 to C_1 products, by increasing the reaction energy barrier of *CO + *H → CHO*, but promotes the conversion of CO_2 to C_{2+} products by lowering the reaction energy barrier of *CO + *CO → OCCO*. Song *et al*. [142] reported that B-doped Cu-Zn catalysts can stabilize Cu^+ under CO_2RR condition by using *in situ* Raman spectroscopy. The retained Cu^+ species and the lower overpotential for *OCO formation upon incorporation of Zn, which lead to the excellent conversion of CO_2 to C_{2+} products on B-Cu-Zn GDEs. Patra *et al*. [111] also observed multiple adsorbed CO sites and enhanced *CO adsorption strength on the B-doped $Cu^{\delta+}$ surface by means of *in situ* ATR-SEIRAS, which are the key factors to improve the selectivity of C_{2+} products. Although some studies attributed the enhancement of C_{2+} product selectivity to the stabilization of Cu^+ by B-doping, Li *et al*. [136] found that there's no detectable Cu(I) species in electroplated Cu-B electrode *via* combined X-ray photoelectron spectroscopy and synchrotron radiated absorption spectroscopy. The authors suggested that the B doping affects the binding energy of Cu-CO and promotes the generation rate of C_{2+} products. *In situ* ATR-SEIRAS results revealed a more facile conversion/depletion of the *CO intermediate after B-doping, correlating the rate of *CO consumption with C_{2+} partial current at molecular level.

6. Electrolyte effect on CO_2RR

The catalytic selectivity and activity of electrochemical interfaces can be affected by the supporting electrolyte ions. It has been shown that with increasing radius of alkali metal cation, the CO_2RR reactivity was significantly improved, especially the current density and the selectivity of C_{2+}

products [143]. Some studies suggest that the influence of cations on CO_2RR reflects the changes in the local microenvironment, such as local electric field strength, interfacial CO_2 concentration, interfacial pH, etc [144–149]. The electrostatic interaction between cations and adsorbed species has been suggested to stabilize reaction intermediates [150,151]. In addition to acting as a buffer, the anions in the electrolyte can also be specifically adsorbed on the electrode surface, affecting the coverage of CO and changing the selectivity of the products [152]. It has also been reported that bicarbonate participates in the CO_2RR reaction [34,55,153]. This subsection summarizes the application of *in situ* vibrational spectroscopies in the understanding of ion effects on the electrocatalytic CO_2RR.

6.1. Cation effect

Gunathunge *et al.* [149] applied *in situ* infrared spectroscopy to monitor the effects of alkali metal cations on CO coverage and local electric field strength on polycrystalline Cu electrodes (Fig. 11(a)). It was found that in electrolytes containing K^+ and Cs^+, ν_{CO} shifted to lower frequencies compared to that in electrolytes containing Li^+ (Fig. 11(b)). This observation suggests that with the increase of the size of the alkali metal cation, the local electric field also increases, which induces a red shift of the C≡O stretching frequency. At higher overpotentials, in electrolytes containing K^+ and Cs^+, the CO coverage on Cu electrodes decreased significantly until approaching 0. while in Li^+ electrolytes, the CO coverage remained ~0.5. This observation indicates that CORR reaction rate is accelerated in the electrolyte containing K^+ and Cs^+. This finding provides a strategy to improve the catalytic selectivity of CO_2RR on metal electrodes with poor selectivity.

Malkani *et al.* [145] and Ayemoba *et al.* [154] followed the model proposed by Singh *et al.* [148] for cation-enhanced CO_2RR, estimating the interfacial local pH and CO_2 concentration by *in situ* infrared spectroscopy. By integrating the peak intensities of dissolved CO_2 (2340 cm^{-1}) and bicarbonate (1650 cm^{-1}), Ayemoba *et al.* [154] calculated the local pH near Au electrodes in the presence of different alkali metal cations (Fig. 11(c,d)). The results show that Li^+ has a much lower buffering capacity than Cs^+, because the hydrolysis pKa of Cs^+ is smaller than that of Li^+, which experimentally verifies Singh's simulation results. However, Malkani *et al.* [145] found that the local CO_2 concentration near Au electrodes decreased with the increase of alkali metal cation radius, contradicting the predictions of Singh *et al.* based on the interfacial pKa theory. Compared with other alkali metal cations, the local CO_2 concentration near Au electrodes is the lowest in the electrolytes containing Cs^+, which was explained in terms of rapid conversion of CO_2 to CO in the presence of Cs^+.

Alkali metal cations were also reported to stabilize CO_2RR-generated intermediates. Pérez-Gallent *et al.* [151] found that at low overpotentials in alkaline electrolytes containing Li^+, Na^+, and K^+, the hydrogenation dimer (*OCCOH) existed as indicated by the observation of a peak at 1191 cm^{-1}

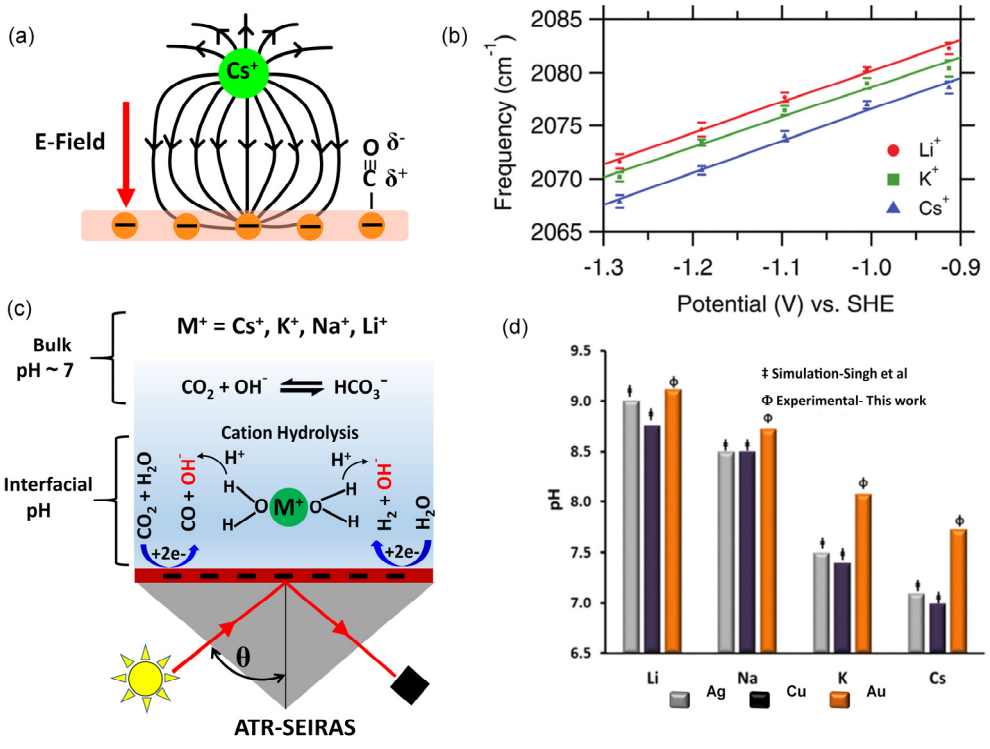

Fig. 11. (a) Schematic illustration of the effect of alkali metal cations on the local interfacial electric field on Cu electrodes. (b) Peak frequencies of the C≡O stretch band of linearly-bonded CO as a function of applied potential in CO-saturated 0.1 mol/L alkali metal bicarbonates as indicated. Reprinted with permission from Ref. [149]. Copyright 2017, The Royal Society of Chemistry. (c) Schematic illustration of the effect of alkali metal cations on local pH on Cu electrodes. (d) Steady-state pH at the metal-electrolyte interface during the electroreduction of CO_2 at –1.0 V *vs.* RHE in CO_2-saturated 0.05 mol/L M_2CO_3 solutions (M = Li^+, Na^+, K^+, Cs^+). Reprinted with permission from Ref. [154]. Copyright 2017, American Chemical Society.

attributed to the stretching vibration of CO in the dimer. However, in Rb^+ or Cs^+-containing solution, this peak was not detected. The C–O stretching band intensity of the hydrogenated dimer decreases from Li^+ to K^+, indicating that the formation of this intermediate depends on the size of the cation. For Rb^+ and Cs^+, a new peak appeared at 1407 cm^{-1}, which may be assigned to formaldehyde. DFT calculations show that the cations enhance the adsorption of C–C containing species more than that of the C1 intermediate, lowering the energy barrier for the reductive coupling of *CO. In addition, larger cations such as Cs^+ can stabilize C_{2+} intermediates more efficiently than smaller cations (Li^+). Recent experimental results by Monteiro *et al*. [155] and Ye *et al*. [156] also suggested that partially desolvated metal cations stabilize CO_2-intermediates through short-range electrostatic interactions, thereby promoting CO_2 reduction.

In addition to the size effect of cations, the concentration of cations affects the CO_2RR reactivity. Li *et al*. [157] found that by adding $NaClO_4$ to increase the concentration of Na^+ in 0.1 mol/L NaOH solution while maintaining the bulk pH of the electrolyte, the partial current density and FE of C_{2+} products were significantly increased. The authors concluded that in alkaline electrolytes, high concentration of Na^+ is the key to improving CO_2RR performance rather than high concentration of OH^-. This is different from the traditional view that "electrolyte pH affects the reaction kinetics of CO/CO_2RR". The authors used crown ether to chelate Na^+ in the solution to keep the OH^- of the solution unchanged while reduce the free Na^+ concentration, and the partial current density and FE of the C_{2+} product decreased significantly, confirming the Na^+ concentration effect. No obvious change in the Stark tuning rate of CO adsorbed on Cu with increasing Na^+ concentration was observed in the infrared spectra, which rules out the influence of specific adsorption of cations or change in electric field strength on product selectivity.

Cations also alter the CO_2RR reactivity by affecting the structure of interfacial water that interacts with electrode. Li *et al*. [158] used bulky tetraalkyl quaternary ammonium cations to study the effect of the electrode and interfacial water interaction on CO_2RR performance. In the CO-saturated electrolyte with D_2O, a peak at 2710 cm^{-1} was observed owing to the formation of O–D bonds between CO adsorbed on the Cu electrode and interfacial D_2O. The peak intensity of O–D stretch decreases with the increase of the quaternary ammonium cation radius until it disappears. It was concluded that larger quaternary ammonium cations replace the water layer, blocking the interaction of adsorbed CO with interfacial water. Hussain *et al*. [146] also confirmed the conclusion by combining infrared spectroscopy and AMID simulation method, revealing that cations affect the orientation of the interfacial water dipole, which results in different hydrogen bonding between the interfacial water and the adsorbed CO intermediate.

6.2. Anion effect

Bicarbonate plays an important role in the CO_2RR process as a common electrolyte, acting as a pH buffer and a proton donor [159]. Recently, Zhu *et al*. [59] provided new insights into the reaction mechanism and origin of bicarbonate effect in CO_2RR on Cu electrodes by *in situ* ATR-SEIRAS in conjunction with isotope labeling. CO_2RR was performed at –0.6 V *vs*. RHE in a 0.1 mol/L $KH^{13}CO_3$ solution saturated with $^{12}CO_2$. The time-resolved IR spectra revealed the consumed $^{13}CO_2$ (2277 cm^{-1}) and generated adsorbed ^{13}CO (2005 cm^{-1}) peaks appeared first, and then the peaks for $^{12}CO_2$ (2343 cm^{-1}) and $*^{12}CO$ (2052 cm^{-1}) showed up, indicating that the CO_2 involved in the reaction on the Cu surface comes from the rapid exchange of near-surface bicarbonate and solution-phase CO_2, rather than directly from the bulk solution. Dunwell *et al*. [160] found that bicarbonate is the main carbon source for CO production on Au electrodes through the exchange equilibrium of bicarbonate with dissolved CO_2.

In the CO_2RR process, with the negative shift of the potential, both the hydrogen evolution reaction and the CO_2RR require the participation of protons, resulting in the rapid consumption of H^+ on the electrode surface and the dramatic change of the local pH near the electrode [161]. Anions with buffering ability are often used as electrolytes. Yang *et al*. [161] monitored the local pH near electrodes in phosphate electrolytes with strong buffering capacity by *in situ* infrared spectroscopy. In CO_2-saturated 0.2 mol/L phosphate ($H_2PO_4^-$/HPO_4^{2-}) buffer solutions, the phosphate buffer showed almost no apparent buffer region, and the local pH also increased significantly with increasing current density. This demonstrates that even a strong buffer such as phosphate solutions cannot maintain the local pH. The high local pH leads to the direct reaction of liquid-phase CO_2 with OH^- to generate carbonate species, resulting in a dramatic decrease in CO_2 concentration rather which hinders CO_2RR. Therefore, mass transport needs to be enhanced when evaluating the intrinsic activity and kinetic parameters of CO_2RR.

In addition to using buffering anions as electrolytes, anions with specific adsorption such as halogens are also used in the CO_2RR reaction. For example, Gao *et al*. [162] found that in electrolytes containing I^-, CuI crystals with specific morphology were spontaneously formed on the surface of the copper oxide catalyst, and part of the CuI could exist stably during the CO_2RR process. Under such conditions, more reactive surface Cu^+ species was introduced, and at the same time highly rough catalyst surfaces were formed on which CO adsorption is much stronger. These electrolyte-induced catalyst structural changes were taken as the reasons for the high selectivity of CO_2RR to multicarbon products. Using infrared spectroscopy, Ovalle *et al*. [163] found that high concentration of Cl^- would compet with CO to adsorb on Cu, which in turn affect the structure of the Cu electrode, the adsorption configuration of CO, and the coverage of CO. However, lacking direct spectroscopic evidence, the authors did not correlate the effects of anions on CO coverage with CO_2RR products.

7. Summary and outlook

This review summarizes the applications of *in situ* electro-

chemical vibrational spectroscopies to the fundamental aspects related to CO_2RR, by elucidating the reaction intermediates involved in different pathways, the effects of catalyst, electrolyte and adsorbed CO on directing reaction selectivity and activity. It should be noted that solid assignments of observed spectra feature and reactive intermediates rely on the advanced theoretical simulations, careful isotope labeling and comprehensive spectroelectrochemical validation. The complexity of CO_2RR presents many more challenges and opportunities for future research in this field and our understanding of this system is far from satisfactory. To end this review, we put forward the following outlooks for the implementation of *in situ* vibrational spectroscopy toward deeper understanding of CO_2RR:

7.1. Developing high-sensitivity wide-frequency vibrational spectroscopy for the fingerprint analysis of intermediates

Among all *in situ* characterization techniques, *in situ* vibrational spectroscopy can directly capture CO_2RR reaction intermediates and reveal the reaction pathway. However, its application also bears limitations. Taken infrared spectra as an example, when Si is used as the IR window, the absorption peak of Si–O at ~1200 cm^{-1} and the significant optical absorption below ~1000 cm^{-1} largely hinder reliable assignments of surface adsorbed C_{2+} species. Therefore, developing high-quality and wide-frequency vibrational spectroelectrochemical methods is highly desirable for tracking the dynamic behavior of key intermediate inter-conversion during CO_2RR.

7.2. Coupling spectroelectrochemical methods toward deeper understanding of the structure-performance relationship of CO_2RR catalysts

As discussed above, each spectroscopic method could capture some pieces of CO_2RR information, while a comprehensive understanding of the CO_2RR mechanism as well as the complex structure-performance relationship relies on the combination of multiple *in situ* spectroelectrochemcial approaches and theoretical simulations. For example, combine *in situ* IR, Raman spectroscopies and online mass spectrometry to monitor adsorbed and non-adsorbed key intermediate species and products of CO_2RR; combine theoretical calculation methods with experimental results to clarify the reaction process and establish the relationship between surface interfaces/species, and reaction selectivity/activity; use X-ray spectroscopy characterization (operando X-ray absorption spectroscopy, X-ray photoelectron spectroscopy, etc.) to analyze the structural changes of electrocatalyst, valence state, lattice structure, coordination structure, density of defect sites, etc.

7.3. Implementing operando vibrational spectroscopies in CO_2RR electrolyzers

So far, most of the reported vibrational spectroscopic studies on CO_2RR have been carried out in H-type electrolyzers at a current density of milli-amps, whereas mechanistic investigations of operando CO_2RR under industrial-scale reaction rate (current density) are lacking. Therefore, it is necessary to develop spectroelectrochemical techniques in gas diffusion electrode under operando conditions of MEA electrolyzer, studying the effect of the membrane electrode structure on the CO_2RR activity and selectivity, and correlating the real-time tri-phase boundary information with the observed CO_2RR performance. The feedback loop between molecular level understandings and the MEA performance at operando CO_2RR conditions could aid the development of more efficient electrolyzer reactors.

References

[1] O. S. Bushuyev, P. De Luna, C. T. Dinh, L. Tao, G. Saur, J. Van De Lagemaat, S. O. Kelley, E. H. Sargent, *Joule*, **2018**, 2, 825–832.
[2] J. Resasco, A. T. Bell, *Trends Chem.*, **2020**, 2, 825–836.
[3] X. Zhao, L. Du, B. You, Y. Sun, *Catal. Sci. Technol.*, **2020**, 10,

Graphical Abstract

Chin. J. Catal., 2022, 43: 0–0 doi: 10.1016/S1872-2067(22)64095-6

Fundamental aspects in CO_2 electroreduction reaction and solutions from *in situ* vibrational spectroscopies

Hong Li, Kun Jiang, Shou-Zhong Zou *, Wen-Bin Cai *
Fudan University, China; Shanghai Jiao Tong University, China; American University, USA

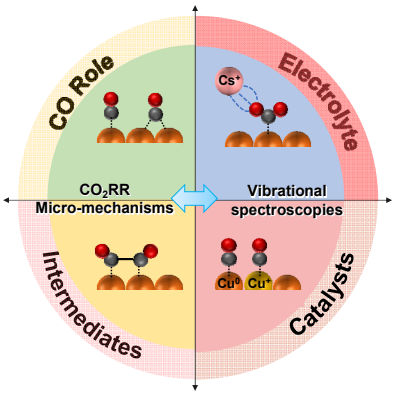

This review summarizes representative results of *in situ* vibrational spectroscopic studies on key fundamental issues in CO_2 electroreduction reaction and gives an outlook for future investigations.

2711–2720.
[4] Y. Y. Birdja, E. Pérez-Gallent, M. C. Figueiredo, A. J. Göttle, F. Calle-Vallejo, M. T. M. Koper, *Nat. Energy*, **2019**, 4, 732–745.
[5] G. Wang, J. Chen, Y. Ding, P. Cai, L. Yi, Y. Li, C. Tu, Y. Hou, Z. Wen, L. Dai, *Chem. Soc. Rev.*, **2021**, 50, 4993–5061.
[6] F. Liang, K. Zhang, L. Zhang, Y. Zhang, Y. Lei, X. Sun, *Small*, **2021**, 17, 2100323.
[7] M. G. Kibria, J. P. Edwards, C. M. Gabardo, C. T. Dinh, A. Seifitokaldani, D. Sinton, E. H. Sargent, *Adv. Mater.*, **2019**, 31, 1807166.
[8] D. Gao, R. M. Arán-Ais, H. S. Jeon, B. Roldan Cuenya, *Nat. Catal.*, **2019**, 2, 198–210.
[9] F. Franco, C. Rettenmaier, H. S. Jeon, B. Roldan Cuenya, *Chem. Soc. Rev.*, **2020**, 49, 6884–6946.
[10] Y. Wang, J. Liu, G. Zheng, *Adv. Mater.*, **2021**, 33, 2005798.
[11] L. Zhang, Z. J. Zhao, J. Gong, *Angew. Chem. Int. Ed.*, **2017**, 56, 11326–11353.
[12] S. Zhu, M. Shao, *J. Solid. State. Electrochem.*, **2015**, 20, 861–873.
[13] S. Nitopi, E. Bertheussen, S. B. Scott, X. Liu, A. K. Engstfeld, S. Horch, B. Seger, I. E. L. Stephens, K. Chan, C. Hahn, J. K. Norskov, T. F. Jaramillo, I. Chorkendorff, *Chem. Rev.*, **2019**, 119, 7610–7672.
[14] C. Liu, J. Gong, Z. Gao, L. Xiao, G. Wang, J. Lu, L. Zhuang, *Sci. China Chem.*, **2021**, 64, 1660–1678.
[15] B. Deng, M. Huang, X. Zhao, S. Mou, F. Dong, *ACS Catal.*, **2021**, 12, 331–362.
[16] S. Sharifi Golru, E. J. Biddinger, *Chem. Eng. J.*, **2022**, 428, 131303.
[17] A. J. Garza, A. T. Bell, M. Head-Gordon, *ACS Catal.*, **2018**, 8, 1490–1499.
[18] L. R. L. Ting, B. S. Yeo, *Curr. Opin. Electrochem.*, **2018**, 8, 126–134.
[19] W. Ma, X. He, W. Wang, S. Xie, Q. Zhang, Y. Wang, *Chem. Soc. Rev.*, **2021**, 50, 12897–12914.
[20] P. Zhu, H. Wang, *Nat. Catal.*, **2021**, 4, 943–951.
[21] E. W. Lees, B. A. W. Mowbray, F. G. L. Parlane, C. P. Berlinguette, *Nat. Rev. Mater.*, **2022**, 7, 55–64.
[22] C. T. Dinh, T. Burdyny, M. G. Kibria, A. Seifitokaldani, C. M. Gabardo, F. P. G. De Arquer, A. Kiani, J. P. Edwards, P. De Luna, O. S. Bushuyev, C. Q. Zou, R. Quintero-Bermudez, Y. J. Pang, D. Sinton, E. H. Sargent, *Science*, **2018**, 360, 783–787.
[23] J. Wang, F. Zhang, X. Kang, S. Chen, *Curr. Opin. Electrochem.*, **2019**, 13, 40–46.
[24] J. Timoshenko, B. Roldan Cuenya, *Chem. Rev.*, **2021**, 121, 882–961.
[25] X. Li, S. Wang, L. Li, Y. Sun, Y. Xie, *J. Am. Chem. Soc.*, **2020**, 142, 9567–9581.
[26] A. D. Handoko, F. Wei, Jenndy, B. S. Yeo, Z. W. Seh, *Nat. Catal.*, **2018**, 1, 922–934.
[27] S. Ye, T. Kondo, N. Hoshi, J. Inukai, S. Yoshimoto, M. Osawa, K. Itaya, *Electrochemistry*, **2009**, 77, 2–20.
[28] X. Cao, D. Tan, B. Wulan, K. S. Hui, K. N. Hui, J. Zhang, *Small Methods*, **2021**, 5, 2100700.
[29] N. Heidary, K. H. Ly, N. Kornienko, *Nano Lett.*, **2019**, 19, 4817–4826.
[30] H. Wang, Y.-W. Zhou, W.-B. Cai, *Curr. Opin. Electrochem.*, **2017**, 1, 73–79.
[31] L. Jin, A. Seifitokaldani, *Catalysts*, **2020**, 10, 481.
[32] P. Zhu, C. Xia, C. Y. Liu, K. Jiang, G. Gao, X. Zhang, Y. Xia, Y. Lei, H. N. Alshareef, T. P. Senftle, H. Wang, *Proc. Natl. Acad. Sci. U. S. A.*, **2021**, 118, e2010868118.
[33] A. Kemna, N. García Rey, B. Braunschweig, *ACS Catal.*, **2019**, 9, 6284–6292.
[34] S. Zhu, T. Li, W.-B. Cai, M. Shao, *ACS Energy Lett.*, **2019**, 4, 682–689.
[35] M. Osawa, K. Yoshii, *Appl. Spectrosc.*, **1997**, 51, 512–518.
[36] M. Osawa, Surface-Enhanced Infrared Absorption Spectroscopy. Springer, Singapore, **2018**, 697–706.
[37] Y.-Y. Yang, H.-X. Zhang, W.-B. Cai, *J. Electrochem.*, **2013**, 19, 6–16.
[38] H. Miyake, S. Ye, M. Osawa, *Electrochem. Commun.*, **2002**, 4, 973–977.
[39] S.-J. Huo, X.-K. Xue, Q.-X. Li, S.-F. Xu, W.-B. Cai, *J. Phys. Chem. B*, **2006**, 110, 25721–25728.
[40] H.-F. Wang, Y.-G. Yan, S.-J. Huo, W.-B. Cai, Q.-J. Xu, M. Osawa, *Electrochim. Acta*, **2007**, 52, 5950–5957.
[41] H.-L. Wang, E.-M. You, R. Panneerselvam, S.-Y. Ding, Z.-Q. Tian, *Light-Sci. Appl.*, **2021**, 10, 161.
[42] H.-Q. Chen, L. Zou, D.-Y. Wei, L.-L. Zheng, Y.-F. Wu, H. Zhang, J.-F. Li, *Chin. J. Catal.*, **2022**, 43, 33–46.
[43] J. F. Li, Y. J. Zhang, S. Y. Ding, R. Panneerselvam, Z. Q. Tian, *Chem. Rev.*, **2017**, 117, 5002–5069.
[44] C. Zhan, X. J. Chen, Y. F. Huang, D. Y. Wu, Z. Q. Tian, *Acc. Chem. Res.*, **2019**, 52, 2784–2792.
[45] S. Ye, M. Osawa, K. Uosaki, *J. Vac. Soc. Jpn,.* **2004**, 47, 439–445.
[46] Y. Tong, Y. Zhao, N. Li, M. Osawa, P. B. Davies, S. Ye, *J. Chem. Phys.*, **2010**, 133, 034705.
[47] S. Wallentine, S. Bandaranayake, S. Biswas, L. R. Baker, *J. Phys. Chem. A*, **2020**, 124, 8057–8064.
[48] Y. Hori, in: *Modern Aspects of Electrochemistry*, C. G. Vayenas, R. E. White, M. E. Gamboa-Aldeco, Ed, Springer, New York, **2008**, 89–189.
[49] A. Bagger, W. Ju, A. S. Varela, P. Strasser, J. Rossmeisl, *ChemPhysChem*, **2017**, 18, 3266–3273.
[50] Y. Katayama, F. Nattino, L. Giordano, J. Hwang, R. R. Rao, O. Andreussi, N. Marzari, Y. Shao-Horn, *J. Phys. Chem. C*, **2018**, 123, 5951–5963.
[51] T. Cheng, A. Fortunelli, W. A. Goddard, III, *Proc. Natl. Acad. Sci. U. S. A.*, **2019**, 116, 7718–7722.
[52] K. Jiang, Y. Huang, G. Zeng, F. M. Toma, W. A. Goddard, III, A. T. Bell, *ACS Energy Lett.*, **2020**, 5, 1206–1214.
[53] M. F. Baruch, J. E. Pander, J. L. White, A. B. Bocarsly, *ACS Catal.*, **2015**, 5, 3148–3156.
[54] J. E. Pander, M. F. Baruch, A. B. Bocarsly, *ACS Catal.*, **2016**, 6, 7824–7833.
[55] C. Cao, D. D. Ma, J. F. Gu, X. Xie, G. Zeng, X. Li, S. G. Han, Q. L. Zhu, X. T. Wu, Q. Xu, *Angew. Chem. Int. Ed.*, **2020**, 59, 15014–15020.
[56] A. Dutta, A. Kuzume, M. Rahaman, S. Vesztergom, P. Broekmann, *ACS Catal.*, **2015**, 5, 7498–7502.
[57] K. R. Phillips, Y. Katayama, J. Hwang, Y. Shao-Horn, *J. Phys. Chem. Lett.*, **2018**, 9, 4407–4412.
[58] A. Dutta, I. Zelocualtecatl Montiel, K. Kiran, A. Rieder, V. Grozovski, L. Gut, P. Broekmann, *ACS Catal.*, **2021**, 11, 4988–5003.
[59] S. Zhu, B. Jiang, W. B. Cai, M. Shao, *J. Am. Chem. Soc.*, **2017**, 139, 15664–15667.
[60] E. Pérez-Gallent, M. C. Figueiredo, F. Calle-Vallejo, M. T. Koper, *Angew. Chem. Int. Ed.*, **2017**, 56, 3621–3624.
[61] K. P. Kuhl, T. Hatsukade, E. R. Cave, D. N. Abram, J. Kibsgaard, T. F. Jaramillo, *J. Am. Chem. Soc.*, **2014**, 136, 14107–14113.
[62] S. Jin, Z. Hao, K. Zhang, Z. Yan, J. Chen, *Angew. Chem. Int. Ed.*, **2021**, 60, 20627–20648.
[63] N. J. Firet, W. A. Smith, *ACS Catal.*, **2017**, 7, 606–612.
[64] W. Shan, R. Liu, H. Zhao, Z. He, Y. Lai, S. Li, G. He, J. Liu, *ACS Nano*, **2020**, 14, 11363–11372.
[65] B. Braunschweig, P. Mukherjee, J. L. Haan, D. D. Dlott, *J. Electroanal. Chem.*, **2017**, 800, 144–150.
[66] M. Dunwell, W. Luc, Y. Yan, F. Jiao, B. Xu, *ACS Catal.*, **2018**, 8, 8121–8129.
[67] S. Wallentine, S. Bandaranayake, S. Biswas, L. R. Baker, *J. Phys. Chem. Lett.*, **2020**, 11, 8307–8313.

[68] B. A. Rosen, A. Salehi-Khojin, M. R. Thorson, W. Zhu, D. T. Whipple, P. J. A. Kenis, R. I. Masel, *Science*, **2011**, 334, 643–644.
[69] N. García Rey, D. D. Dlott, *J. Phys. Chem. C*, **2015**, 119, 20892–20899.
[70] B. A. Rosen, J. L. Haan, P. Mukherjee, B. Braunschweig, W. Zhu, A. Salehi-Khojin, D. D. Dlott, R. I. Masel, *J. Phys. Chem. C*, **2012**, 116, 15307–15312.
[71] R. Kortlever, J. Shen, K. J. Schouten, F. Calle-Vallejo, M. T. M. Koper, *J. Phys. Chem. Lett.*, **2015**, 6, 4073–4082.
[72] A. Vasileff, Y. Zhu, X. Zhi, Y. Zhao, L. Ge, H. M. Chen, Y. Zheng, S. Z. Qiao, *Angew. Chem. Int. Ed.*, **2020**, 59, 19649–19653.
[73] Y. Kim, S. Park, S.-J. Shin, W. Choi, B. K. Min, H. Kim, W. Kim, Y. J. Hwang, *Energy Environ. Sci.*, **2020**, 13, 4301–4311.
[74] W. Ma, S. Xie, T. Liu, Q. Fan, J. Ye, F. Sun, Z. Jiang, Q. Zhang, J. Cheng, Y. Wang, *Nat. Catal.*, **2020**, 3, 478–487.
[75] J. Li, X. Chang, H. Zhang, A. S. Malkani, M. J. Cheng, B. Xu, Q. Lu, *Nat. Commun.*, **2021**, 12, 3264.
[76] A. D. Handoko, K. W. Chan, B. S. Yeo, *ACS Energy Lett.*, **2017**, 2, 2103–2109.
[77] M. Ma, K. Djanashvili, W. A. Smith, *Angew. Chem. Int. Ed.*, **2016**, 55, 6680–6684.
[78] K. D. Yang, W. R. Ko, J. H. Lee, S. J. Kim, H. Lee, M. H. Lee, K. T. Nam, *Angew. Chem. Int. Ed.*, **2017**, 56, 796–800.
[79] A. Dutta, M. Rahaman, N. C. Luedi, M. Mohos, P. Broekmann, *ACS Catal.*, **2016**, 6, 3804–3814.
[80] Z. C. Huang-Fu, Q. T. Song, Y. H. He, J. J. Wang, J. Y. Ye, Z. Y. Zhou, S. G. Sun, Z. H. Wang, *Phys. Chem. Chem. Phys.*, **2019**, 21, 25047–25053.
[81] C. M. Gunathunge, J. Li, X. Li, M. M. Waegele, *ACS Catal.*, **2020**, 10, 11700–11711.
[82] C. M. Gunathunge, V. J. Ovalle, Y. Li, M. J. Janik, M. M. Waegele, *ACS Catal.*, **2018**, 8, 7507–7516.
[83] F. Li, A. Thevenon, A. Rosas-Hernandez, Z. Wang, Y. Li, C. M. Gabardo, A. Ozden, C. T. Dinh, J. Li, Y. Wang, J. P. Edwards, Y. Xu, C. Mccallum, L. Tao, Z. Q. Liang, M. Luo, X. Wang, H. Li, C. P. O'brien, C. S. Tan, D. H. Nam, R. Quintero-Bermudez, T. T. Zhuang, Y. C. Li, Z. Han, R. D. Britt, D. Sinton, T. Agapie, J. C. Peters, E. H. Sargent, *Nature*, **2020**, 577, 509–513.
[84] A. Wuttig, M. Yaguchi, K. Motobayashi, M. Osawa, Y. Surendranath, *Proc. Natl. Acad. Sci. U. S. A.*, **2016**, 113, E4585–E4593.
[85] T.-W. Jiang, Y.-W. Zhou, X.-Y. Ma, X. Qin, H. Li, C. Ding, B. Jiang, K. Jiang, W.-B. Cai, *ACS Catal.*, **2021**, 11, 840–848.
[86] T. C. Chou, C. C. Chang, H. L. Yu, W. Y. Yu, C. L. Dong, J. J. Velasco-Velez, C. H. Chuang, L. C. Chen, J. F. Lee, J. M. Chen, H. L. Wu, *J. Am. Chem. Soc.*, **2020**, 142, 2857–2867.
[87] X. Chang, Y. Zhao, B. Xu, *ACS Catal.*, **2020**, 10, 13737–13747.
[88] C. Zhan, F. Dattila, C. Rettenmaier, A. Bergmann, S. Kühl, R. García-Muelas, N. López, B. R. Cuenya, *ACS Catal.*, **2021**, 11, 7694–7701.
[89] A. Wuttig, C. Liu, Q. Peng, M. Yaguchi, C. H. Hendon, K. Motobayashi, S. Ye, M. Osawa, Y. Surendranath, *ACS Cent. Sci.*, **2016**, 2, 522–528.
[90] C. M. Gunathunge, X. Li, J. Li, R. P. Hicks, V. J. Ovalle, M. M. Waegele, *J. Phys. Chem. C*, **2017**, 121, 12337–12344.
[91] Z. Li, Y. Yang, Z. Yin, X. Wei, H. Peng, K. Lyu, F. Wei, L. Xiao, G. Wang, H. D. Abruña, J. Lu, L. Zhuang, *ACS Catal.*, **2021**, 11, 2473–2482.
[92] A. Wuttig, J. Ryu, Y. Surendranath, *J. Phys. Chem. C*, **2021**, 125, 17042–17050.
[93] A. S. Malkani, J. Li, J. Anibal, Q. Lu, B. Xu, *ACS Catal.*, **2019**, 10, 941–946.
[94] C. M. Gunathunge, J. Li, X. Li, J. J. Hong, M. M. Waegele, *ACS Catal.*, **2020**, 10, 6908–6923.
[95] G. Iijima, T. Inomata, H. Yamaguchi, M. Ito, H. Masuda, *ACS Catal.*, **2019**, 9, 6305–6319.
[96] G. Iijima, H. Yamaguchi, T. Inomata, H. Yoto, M. Ito, H. Masuda, *ACS Catal.*, **2020**, 10, 15238–15249.
[97] A. S. Malkani, M. Dunwell, B. Xu, *ACS Catal.*, **2019**, 9, 474–478.
[98] H. An, L. Wu, L. D. B. Mandemaker, S. Yang, J. De Ruiter, J. H. J. Wijten, J. C. L. Janssens, T. Hartman, W. Van Der Stam, B. M. Weckhuysen, *Angew. Chem. Int. Ed.*, **2021**, 60, 16576–16584.
[99] C. W. Li, M. W. Kanan, *J. Am. Chem. Soc.*, **2012**, 134, 7231–7234.
[100] C. W. Li, J. Ciston, M. W. Kanan, *Nature*, **2014**, 508, 504–507.
[101] A. Verdaguer-Casadevall, C. W. Li, T. P. Johansson, S. B. Scott, J. T. Mckeown, M. Kumar, I. E. Stephens, M. W. Kanan, I. Chorkendorff, *J. Am. Chem. Soc.*, **2015**, 137, 9808–9811.
[102] S. Y. Lee, H. Jung, N. K. Kim, H. S. Oh, B. K. Min, Y. J. Hwang, *J. Am. Chem. Soc.*, **2018**, 140, 8681–8689.
[103] Y. Zhou, F. Che, M. Liu, C. Zou, Z. Liang, P. De Luna, H. Yuan, J. Li, Z. Wang, H. Xie, H. Li, P. Chen, E. Bladt, R. Quintero-Bermudez, T. K. Sham, S. Bals, J. Hofkens, D. Sinton, G. Chen, E. H. Sargent, *Nat. Chem.*, **2018**, 10, 974–980.
[104] C. Chen, X. Sun, L. Lu, D. Yang, J. Ma, Q. Zhu, Q. Qian, B. Han, *Green Chem.*, **2018**, 20, 4579–4583.
[105] W. Zhang, P. He, C. Wang, T. Ding, T. Chen, X. Liu, L. Cao, T. Huang, X. Shen, O. A. Usoltsev, A. L. Bugaev, Y. Lin, T. Yao, *J. Mater. Chem. A*, **2020**, 8, 25970–25977.
[106] Q. Fan, X. Zhang, X. Ge, L. Bai, D. He, Y. Qu, C. Kong, J. Bi, D. Ding, Y. Cao, X. Duan, J. Wang, J. Yang, Y. Wu, *Adv. Energy Mater.*, **2021**, 11, 2101424.
[107] Z. Chen, T. Wang, B. Liu, D. Cheng, C. Hu, G. Zhang, W. Zhu, H. Wang, Z. J. Zhao, J. Gong, *J. Am. Chem. Soc.*, **2020**, 142, 6878–6883.
[108] D. Zhong, Z. J. Zhao, Q. Zhao, D. Cheng, B. Liu, G. Zhang, W. Deng, H. Dong, L. Zhang, J. Li, J. Li, J. Gong, *Angew. Chem. Int. Ed.*, **2021**, 60, 4879–4885.
[109] Z. Z. Wu, X. L. Zhang, Z. Z. Niu, F. Y. Gao, P. P. Yang, L. P. Chi, L. Shi, W. S. Wei, R. Liu, Z. Chen, S. Hu, X. Zheng, M. R. Gao, *J. Am. Chem. Soc.*, **2021**, 144, 259–269.
[110] K. Jiang, R. B. Sandberg, A. J. Akey, X. Liu, D. C. Bell, J. K. Nørskov, K. Chan, H. Wang, *Nat. Catal.*, **2018**, 1, 111–119.
[111] K. K. Patra, S. Park, H. Song, B. Kim, W. Kim, J. Oh, *ACS Appl. Energ. Mater.*, **2020**, 3, 11343–11349.
[112] P. De Luna, R. Quintero-Bermudez, C.-T. Dinh, M. B. Ross, O. S. Bushuyev, P. Todorović, T. Regier, S. O. Kelley, P. Yang, E. H. Sargent, *Nat. Catal.*, **2018**, 1, 103–110.
[113] P. P. Yang, X. L. Zhang, F. Y. Gao, Y. R. Zheng, Z. Z. Niu, X. Yu, R. Liu, Z. Z. Wu, S. Qin, L. P. Chi, Y. Duan, T. Ma, X. S. Zheng, J. F. Zhu, H. J. Wang, M. R. Gao, S. H. Yu, *J. Am. Chem. Soc.*, **2020**, 142, 6400–6408.
[114] X. Feng, K. Jiang, S. Fan, M. W. Kanan, *ACS Cent. Sci.*, **2016**, 2, 169–174.
[115] H. Jung, S. Y. Lee, C. W. Lee, M. K. Cho, D. H. Won, C. Kim, H. S. Oh, B. K. Min, Y. J. Hwang, *J. Am. Chem. Soc.*, **2019**, 141, 4624–4633.
[116] C. Chen, X. Sun, X. Yan, Y. Wu, M. Liu, S. Liu, Z. Zhao, B. Han, *Green Chem.*, **2020**, 22, 1572–1576.
[117] R. Kas, R. Kortlever, A. Milbrat, M. T. Koper, G. Mul, J. Baltrusaitis, *Phys. Chem. Chem. Phys.*, **2014**, 16, 12194–12201.
[118] L. Mandal, K. R. Yang, M. R. Motapothula, D. Ren, P. Lobaccaro, A. Patra, M. Sherburne, V. S. Batista, B. S. Yeo, J. W. Ager, J. Martin, T. Venkatesan, *ACS Appl. Mater. Interfaces*, **2018**, 10, 8574–8584.
[119] M. He, C. Li, H. Zhang, X. Chang, J. G. Chen, W. A. Goddard, III, M. J. Cheng, B. Xu, Q. Lu, *Nat. Commun.*, **2020**, 11, 3844.
[120] C. Li, H. Xiong, M. He, B. Xu, Q. Lu, *ACS Catal.*, **2021**, 11, 12029–12037.

[121] W. Deng, L. Zhang, L. Li, S. Chen, C. Hu, Z. J. Zhao, T. Wang, J. Gong, *J. Am. Chem. Soc.*, **2019**, 141, 2911–2915.
[122] P. Iyengar, M. J. Kolb, J. R. Pankhurst, F. Calle-Vallejo, R. Buonsanti, *ACS Catal.*, **2021**, 11, 4456–4463.
[123] L. R. L. Ting, O. Piqué, S. Y. Lim, M. Tanhaei, F. Calle–Vallejo, B. S. Yeo, *ACS Catal.*, **2020**, 10, 4059–4069.
[124] D. Higgins, A. T. Landers, Y. Ji, S. Nitopi, C. G. Morales-Guio, L. Wang, K. Chan, C. Hahn, T. F. Jaramillo, *ACS Energy Lett.*, **2018**, 3, 2947–2955.
[125] L. Xiong, X. Zhang, L. Chen, Z. Deng, S. Han, Y. Chen, J. Zhong, H. Sun, Y. Lian, B. Yang, X. Yuan, H. Yu, Y. Liu, X. Yang, J. Guo, M. H. Rummeli, Y. Jiao, Y. Peng, *Adv. Mater.*, **2021**, 33, 2101741.
[126] A. Herzog, A. Bergmann, H. S. Jeon, J. Timoshenko, S. Kühl, C. Rettenmaier, M. Lopez Luna, F. T. Haase, B. Roldan Cuenya, *Angew. Chem. Int. Ed.*, **2021**, 60, 7426–7435.
[127] E. L. Clark, C. Hahn, T. F. Jaramillo, A. T. Bell, *J. Am. Chem. Soc.*, **2017**, 139, 15848–15857.
[128] T. T. H. Hoang, S. Verma, S. Ma, T. T. Fister, J. Timoshenko, A. I. Frenkel, P. J. A. Kenis, A. A. Gewirth, *J. Am. Chem. Soc.,* **2018**, 140, 5791–5797.
[129] Y. C. Li, Z. Wang, T. Yuan, D. H. Nam, M. Luo, J. Wicks, B. Chen, J. Li, F. Li, F. P. G. De Arquer, Y. Wang, C. T. Dinh, O. Voznyy, D. Sinton, E. H. Sargent, *J. Am. Chem. Soc.*, **2019**, 141, 8584–8591.
[130] D. Ren, B. S.-H. Ang, B. S. Yeo, *ACS Catal.*, **2016**, 6, 8239–8247.
[131] S. Lee, G. Park, J. Lee, *ACS Catal.*, **2017**, 7, 8594–8604.
[132] J. Gao, H. Zhang, X. Guo, J. Luo, S. M. Zakeeruddin, D. Ren, M. Gratzel, *J. Am. Chem. Soc.*, **2019**, 141, 18704–18714.
[133] J. Huang, M. Mensi, E. Oveisi, V. Mantella, R. Buonsanti, *J. Am. Chem. Soc.*, **2019**, 141, 2490–2499.
[134] Z.-J. Sun, M. M. Sartin, W. Chen, F. He, J. Cai, X.-X. Ye, J.-L. Lu, Y.-X. Chen, *Chin. J. Chem. Phys.*, **2020**, 33, 303–310.
[135] H. Li, T.-W. Jiang, X. Qin, J. Chen, X.-Y. Ma, K. Jiang, X.-G. Zhang, W.-B. Cai, *ACS Catal.*, **2021**, 11, 6846–6856.
[136] H. Li, X. Qin, T. Jiang, X. Y. Ma, K. Jiang, W. B. Cai, *ChemCatChem*, **2019**, 11, 6139–6146.
[137] J.-S. Wang, G.-C. Zhao, Y.-Q. Qiu, C.-G. Liu, *J. Phys. Chem. C*, **2020**, 125, 572–582.
[138] T. T. Zhuang, D. H. Nam, Z. Wang, H. H. Li, C. M. Gabardo, Y. Li, Z. Q. Liang, J. Li, X. J. Liu, B. Chen, W. R. Leow, R. Wu, X. Wang, F. Li, Y. Lum, J. Wicks, C. P. O'brien, T. Peng, A. H. Ip, T. K. Sham, S. H. Yu, D. Sinton, E. H. Sargent, *Nat. Commun.*, **2019**, 10, 4807.
[139] Y. Deng, Y. Huang, D. Ren, A. D. Handoko, Z. W. Seh, P. Hirunsit, B. S. Yeo, *ACS Appl. Mater. Interfaces*, **2018**, 10, 28572–28581.
[140] Z. Pan, K. Wang, K. Ye, Y. Wang, H.-Y. Su, B. Hu, J. Xiao, T. Yu, Y. Wang, S. Song, *ACS Catal.*, **2020**, 10, 3871–3880.
[141] D. Liu, Y. Liu, M. Li, *J. Phys. Chem. C*, **2020**, 124, 6145–6153.
[142] Y. Song, J. R. C. Junqueira, N. Sikdar, D. Ohl, S. Dieckhofer, T. Quast, S. Seisel, J. Masa, C. Andronescu, W. Schuhmann, *Angew. Chem. Int. Ed.*, **2021**, 60, 23427–23434.
[143] S. Ringe, E. L. Clark, J. Resasco, A. Walton, B. Seger, A. T. Bell, K. Chan, *Energy Environ. Sci.*, **2019**, 12, 3001–3014.
[144] L. D. Chen, M. Urushihara, K. Chan, J. K. Nørskov, *ACS Catal.*, **2016**, 6, 7133–7139.
[145] A. S. Malkani, J. Anibal, B. Xu, *ACS Catal.*, **2020**, 10, 14871–14876.
[146] G. Hussain, L. Pérez-Martínez, J.-B. Le, M. Papasizza, G. Cabello, J. Cheng, A. Cuesta, *Electrochim. Acta*, **2019**, 327, 135055.
[147] J. Resasco, L. D. Chen, E. Clark, C. Tsai, C. Hahn, T. F. Jaramillo, K. Chan, A. T. Bell, *J. Am. Chem. Soc.*, **2017**, 139, 11277–11287.
[148] M. R. Singh, Y. Kwon, Y. Lum, J. W. Ager, III, A. T. Bell, *J. Am. Chem. Soc.*, **2016**, 138, 13006–13012.
[149] C. M. Gunathunge, V. J. Ovalle, M. M. Waegele, *Phys. Chem. Chem. Phys.*, **2017**, 19, 30166–30172.
[150] H. Liu, J. Liu, B. Yang, *ACS Catal.*, **2021**, 11, 12336–12343.
[151] E. Pérez-Gallent, G. Marcandalli, M. C. Figueiredo, F. Calle-Vallejo, M. T. M. Koper, *J. Am. Chem. Soc.*, **2017**, 139, 16412–16419.
[152] K. Ogura, J. R. Ferrell, A. V. Cugini, E. S. Smotkin, M. D. Salazar-Villalpando, *Electrochim. Acta*, **2010**, 56, 381–386.
[153] W. Deng, T. Yuan, S. Chen, H. Li, C. Hu, H. Dong, B. Wu, T. Wang, J. Li, G. A. Ozin, J. Gong, *Fundamental Res.*, **2021**, 1, 432–438.
[154] O. Ayemoba, A. Cuesta, *ACS Appl. Mater. Interfaces*, **2017**, 9, 27377–27382.
[155] M. C. O. Monteiro, F. Dattila, B. Hagedoorn, R. García-Muelas, N. López, M. T. M. Koper, *Nat. Catal.*, **2021**, 4, 654–662.
[156] K. Ye, G. Zhang, X.-Y. Ma, C. Deng, X. Huang, C. Yuan, G. Meng, W.-B. Cai, K. Jiang, *Energy Environ. Sci.*, **2022**, 15, 749–759.
[157] J. Li, D. Wu, A. S. Malkani, X. Chang, M. J. Cheng, B. Xu, Q. Lu, *Angew. Chem. Int. Ed.*, **2020**, 59, 4464–4469.
[158] J. Li, X. Li, C. M. Gunathunge, M. M. Waegele, *Proc. Natl. Acad. Sci. U. S. A.*, **2019**, 116, 9220–9229.
[159] G. Marcandalli, A. Goyal, M. T. M. Koper, *ACS Catal.*, **2021**, 11, 4936–4945.
[160] M. Dunwell, Q. Lu, J. M. Heyes, J. Rosen, J. G. Chen, Y. Yan, F. Jiao, B. Xu, *J. Am. Chem. Soc.*, **2017**, 139, 3774–3783.
[161] K. Yang, R. Kas, W. A. Smith, *J. Am. Chem. Soc.*, **2019**, 141, 15891–15900.
[162] D. Gao, F. Scholten, B. Roldan Cuenya, *ACS Catal.*, **2017**, 7, 5112–5120.
[163] V. J. Ovalle, M. M. Waegele, *J. Phys. Chem. C*, **2020**, 124, 14713–14721.

CO_2电还原反应中的基础问题及原位振动光谱的对策

李　宏[a], 蒋　昆[b], 邹受忠[c,#], 蔡文斌[a,*]
[a]复旦大学化学系, 能源材料化学协同创新中心, 上海市分子催化与功能材料表面重点实验室, 上海200438, 中国
[b]上海交通大学机械与动力工程学院, 上海200240, 中国
[c]美利坚大学化学系, 华盛顿, 哥伦比亚特区, 美国

摘要: 近年来, 全世界达成了减少温室气体排放、防止气候恶化的共识. 二氧化碳电还原(CO_2RR)是利用可再生能源产生的电能将CO_2气体转化为高能量密度化学品的方案, 可实现CO_2的有效利用和可再生能源的存储, 是实现碳循环的有效途径. CO_2RR过程涉及多个电子转移与质子耦合. 由于该反应体系复杂、中间产物覆盖度低等因素, 电催化机理研究长期以来是个挑战性难题. 同时, CO_2RR过程中催化剂结构演变、活性位点的识别、电解质的作用机制和吸附态CO角色等问题仍存在争议. 原位振动光谱可用于监测界面上CO_2还原反应过程中催化剂结构演变、捕获弱吸附的中间产物, 能够为理清反

应机制和反应路径提供关键信息.

本综述介绍了原位振动光谱包括红外、拉曼和和频光谱等对CO_2RR中关键基本问题的解决策略, 主要包括: (1)揭示了不同电极上CO_2RR的反应中间体和反应路径; (2)探讨了CO在CO_2RR中的角色, 包括CO的吸附构型、覆盖度以及作为分子探针的作用; (3)明确了催化剂(主要Cu基催化剂)的结构与组成对CO_2RR活性和选择性的影响; (4)讨论了CO_2RR过程阴、阳离子对界面局部电场和pH, 以及反应中间体的影响.

CO_2RR过程的复杂性为该领域的研究带来了更多的挑战和机遇, 本文对原位振动光谱的未来发展和应用策略提出以下建议: (1)发展和应用能涵盖指纹区检测的高灵敏宽频红外光谱技术, 获取更多更可靠的中间物种和产物信息; (2)耦合多种原位和在线谱学方法深入揭示CO_2还原催化剂构效关系; (3)发展和应用适合于膜电极体系的振动光谱技术, 探索工况条件下的CO_2RR反应机制.

关键词: 二氧化碳电还原; 电催化机制; 振动光谱; 中间体; 构效关系; 电解质效应

收稿日期: 2022-01-31. 接受日期: 2022-03-27. 上网时间: 2021-00-05.

*通讯联系人. 电话/传真: (021)31244050; 电子信箱: wbcai@fudan.edu.cn

#通讯联系人. 电话/传真: (202)885-1763; 电子信箱: szou@american.edu

基金来源: 国家自然科学基金(21733004,22002088); 上海市“科技创新行动计划”政府间国际科技合作基金项目(17520711200); 上海市青年科技英才扬帆计划(20YF1420500).

本文的电子版全文由Elsevier出版社在ScienceDirect上出版(http://www.sciencedirect.com/journal/chinese-journal-of-catalysis).